Icarus 412 (2024) 115976

Contents lists available at ScienceDirect

Icarus

journal homepage: www.elsevier.com/locate/icarus

Effects of space weathering on the Christiansen feature position of lunar surface materials

Nandita Kumari [a,*], Timothy D. Glotch [a], Katherine A. Shirley [b], Benjamin T. Greenhagen [c], Benjamin D. Byron [d]

[a] Department of Geosciences, Stony Brook University, Stony Brook, NY, United States of America
[b] Department of Atmospheric, Oceanic, and Planetary Physics, University of Oxford, Oxford, UK
[c] Johns Hopkins University Applied Physics Laboratory, Laurel, MD, United States of America
[d] Jet Propulsion Laboratory, California Institute of Technology, Pasadena, CA, United States of America

ARTICLE INFO

Keywords:
Moon
Spectroscopy
Space weathering

ABSTRACT

We use observations by the Lunar Reconnaissance Orbiter Diviner Lunar Radiometer Experiment to examine the effects of space weathering and particle size on the position of the Christiansen feature (CF) in thermal infrared (TIR) spectra of silicate lithologies on the Moon. Laboratory studies have found that both the increased surface iron content associated with formation of nanophase iron (npFe) during space weathering and decreasing grain size of regolith shift the CF position to longer wavelengths for TIR spectra measured under lunar-like conditions. This study confirms that the variation in CF position due to space weathering measured in the laboratory, is also evident at orbital scales. We have used swirls and rayed craters from lunar highlands and mare regions to examine the effect of initial composition and particle size distribution on the change of CF position. We also examine the effect of magnetic shielding at lunar swirls on the CF position. Our observations indicate that 1) for quantitatively comparable changes in albedo, the CF shift is greater for mare surfaces than for highlands surfaces; 2) particle-size is the dominant factor for the CF shift in fine-particulate regolith;3) npFe accumulation dominates CF position changes in coarser regolith and 4) the variation in CF position of lunar swirls is positively correlated to the magnetic field strength in the region. We hypothesize that the effects of particle size variations are also observed between the crater and swirl regions. However, further work is needed to constrain the effective particle size distributions of the regolith.

1. Introduction

Space weathering was first hypothesized by Gold (1955) upon his observation of presence of rays associated with young craters, leading him to conclude that some erosional process must be changing the colour of the surface and thus degrading the appearance of crater rays with time. During the Apollo era, 381 kg of material was returned from the lunar nearside, sampling both highlands and mare material, mostly in the form of breccias (Adams and McCord, 1971; Wilshire and Jackson, 1972; Prinz et al., 1973; Collinson, 1976; Collinson, 1976; Taylor and Siscoe, 1976). These returned samples, along with remote observations, confirmed the phenomenon of space weathering (Pieters et al., 2000; Noble et al., 2007; Pieters and Noble, 2016).

Space weathering is the accumulation of the chemical, physical, structural, and optical changes that mineral grains on airless bodies are subjected to as a result of these processes (Gold, 1955; Zeller and Ronca, 1967; Adams and McCord, 1971; Adams and McCord, 1973; Allen et al., 1993; Hapke, 1998; Dran et al., 1977; Wentworth et al., 1999; Pieters et al., 2000; Noble et al., 2007; Blewett et al., 2010; Glotch et al., 2015; Pieters and Noble, 2016; Poppe et al., 2018). The absence of a global lunar magnetic field (Fuller and Cisowski, 1987; Weiss and Tikoo, 2014; Tikoo et al., 2017; Mighani et al., 2020) and an atmosphere makes the surface vulnerable to the influx of solar wind and cosmic radiation (Poppe et al., 2018). Moreover, the lunar surface is subjected to hypervelocity micrometeoroid impacts.

Space weathering is not limited to the Moon. It has been identified on the surface of Mercury and the bodies in the asteroid belt and near-Earth S-type asteroid populations (Gaffey et al., 1993; Pieters and Noble, 2016; Trang et al., 2017, Trang and Lucey, 2019). However, the relative effects of the various space weathering processes vary with initial

* Corresponding author.
E-mail address: Nandita.kumari@stonybrook.edu (N. Kumari).

https://doi.org/10.1016/j.icarus.2024.115976
Received 28 July 2023; Received in revised form 14 December 2023; Accepted 23 January 2024
Available online 28 January 2024

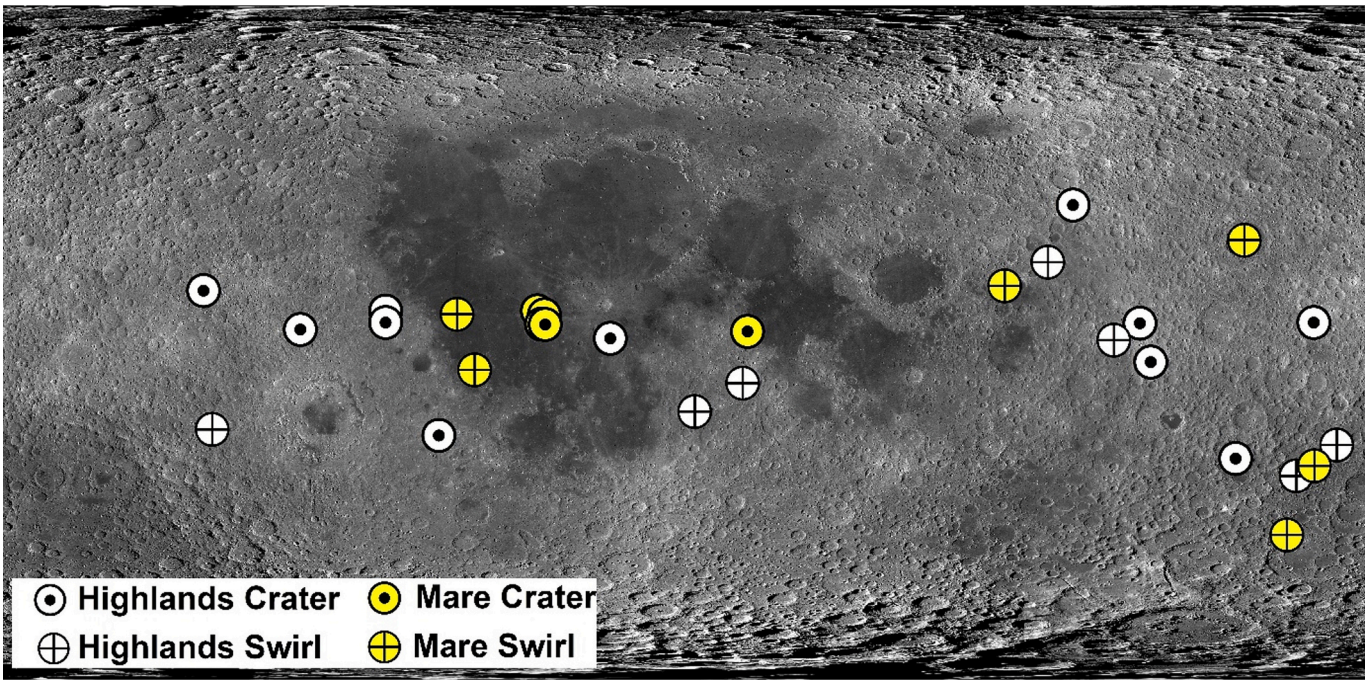

Fig. 1. Global distribution of examined swirls and rayed craters overlayed on LROC-WAC global mosaic

composition and location within the Solar System. The accessibility of the Moon makes it a useful laboratory to understand the optical effects of space weathering and mitigate them in our spectroscopic analyses. Once understood, these optical effects can be mitigated in spectroscopic analyses of other bodies.

The composition of terrestrial surfaces in the inner Solar System is dominated by the presence of silicates (e.g., Bandfield et al., 2000; Greenhagen et al., 2010; Namur and Charlier, 2017). Remote observations and analyses of the returned samples from the Moon have identified pyroxene, olivine, glasses and plagioclase on its surface (Wood et al., 1970; Adams and McCord, 1971; Wilshire and Jackson, 1972; Prinz et al., 1973; Pieters et al., 2009; Greenhagen et al., 2010; Klima et al., 2011; Isaacson et al., 2011; Green et al., 2011; Besse et al., 2014). The two major provinces of the Moon – the maria and highlands – have varied abundances of iron-bearing silicates (e.g., Lucey et al., 2000a, 2000b). While the maria are rich in mafic materials such as pyroxene, olivine, and Fe-bearing glass (e.g., Staid et al., 2011; Klima et al., 2011; Besse et al., 2014); the highlands are dominated by high-Ca plagioclase feldspar (e.g., Smith et al., 1970; Spudis et al., 1984; Ohtake et al., 2008). Silicate minerals display strong vibrational features in the TIR region (~5 μm - 50 μm) (Conel, 1969; Salisbury et al., 1991; Christensen et al., 2000), making TIR spectroscopy a useful tool for bulk identification and quantification of silicate mineralogy. In this wavelength region, silicate minerals display an emissivity maximum known as the Christiansen feature (CF), which corresponds to the wavelength where the real component of the index of refraction passes unity, typically between 7 and 9 μm. The CF position is an indicator of the degree of silicate polymerization within a mineral, occurring at longer wavelengths for less-polymerized mafic silicates and at shorter wavelengths for felsic silicates (Conel, 1969; Logan et al., 1973; Chapman and Salisbury, 1973; Greenhagen et al., 2010). However, laboratory experiments have shown that the position of the CF can be affected by several factors including: particle size, compaction, surface roughness, environment conditions, the visible albedo and thermal gradient (e.g. Logan et al., 1973; Cooper et al., 2002; Lucey et al., 2017; Shirley and Glotch, 2019; Breitenfeld et al., 2021).The LRO Diviner Lunar Radiometer Experiment (Greenhagen et al., 2010; Paige et al., 2010) can be used to estimate the position of the CF of lunar regolith on the lunar surface to study its composition and to investigate the effects of space weathering on TIR spectroscopic measurements.

On airless bodies, due to lack of atmosphere, the heat transfer in the regolith is limited to grain-to-grain contacts and radiation due to the lack of convective heat transfer. This environment results in the formation of a steep thermal gradient within the top few hundreds of microns of the regolith creating a warmer subsurface and cooler surface, which radiates to space (e.g., Henderson and Jakosky, 1997). This is also known as the solid-state greenhouse effect. The position of the CF for silicate minerals shifts to shorter wavelengths under the combined effects of simulated lunar environment (SLE) conditions (e.g. Shirley and Glotch, 2019). Due to this gradient and varying opacity (as a function of wavelength) of the regolith, the net emission has a contribution both from the warm lower layer and cooler top layer leading to a shift in the position of the CF towards shorter wavelengths (Logan et al., 1973; Henderson and Jakosky, 1997; Prem et al., 2022). For instance, the CF of quartz spectra (<32 μm grain size) measured under ambient conditions is identified at 7.385 μm while in SLE it is at 7.173 μm (e.g., Shirley and Glotch, 2019). In a similar manner, the CF of augite spectra (<32 μm grain size) in ambient condition is at 8.474 μm while in SLE, it is at 8.39 μm (e.g., Shirley and Glotch, 2019).

The particle size of a material also has a noticeable effect on spectral contrast and the CF position, due to the variable thermal gradients that are characteristic of different size fractions. Within SLE, decreasing grain size pushes the CF to longer wavelengths. For instance, the CF of augite occurs at 8.39 μm (<32 μm); 8.19 μm (32–63 μm); 8.10 μm (63–90 μm); and 8.09 μm (90–125 μm) (Shirley and Glotch, 2019). Under ambient conditions, a decrease in pore size and an increase in compaction leads to an increase in effective particle size, which eventually lead to scattering loss. Thus, an increase in compaction of particles shifts the CF towards shorter wavelengths under ambient and low-temperature conditions (Logan et al., 1973). The fairy castle sample is a loosely packed porous sample prepared via deposition of material from air elutriation column in Logan et al. (1973). For instance, the CF of quartz (0–5 μm) lies at 7.18 μm for a packed sample and 7.44 μm for a fairy castle sample. The CF of hornblende (0–5 μm) is at 8.47 μm for a packed sample and 8.80 μm for a fairy castle sample (Logan et al., 1973). The dependence of the CF position on these various factors makes it

Table 1
List of all the selected sites, their locations, and the median and standard deviation values for the data on and off the swirl or crater ray. Type: M-Mare, H-Highlands, S-Swirl, C-Crater.

Feature Name	Location	Type	Median CF (On-swirl/ ray) (μm)	Median CF (Off-swirl/ ray) (μm)	Median Albedo (On-swirl/ ray)	Median Albedo (Off- swirl/ ray)
Reiner Gamma	301.04°E, 7.38°N	MS	8.25 ± 0.025	8.31 ± 0.043	0.09 ± 0.007	0.05 ± 0.003
Mare Ingenii	166.04°E, 32.31° S	MS	8.25 ± 0.028	8.28 ± 0.027	0.08 ± 0.006	0.06 ± 0.003
Mare Marginis	84.7°E, 13.04° N	MS	8.26 ± 0.039	8.30 ± 0.053	0.07 ± 0.007	0.06 ± 0.003
Hopmann	160.3°E, 50.8° N	MS	8.19 ± 0.051	8.23 ± 0.032	0.09 ± 0.021	0.07 ± 0.005
Moscoviense Basin*	149.3°E, 26.04° N	MS	8.30 ± 0.093	8.30 ± 0.053	0.07 ± 0.006	0.05 ± 0.002
Sirsalis*	7.1° S, 54.0° W	MS	8.31 ± 0.018	8.30 ± 0.023	0.07 ± 0.004	0.05 ± 0.002
Van de Graaf	172.0°E, 27.04° S	HS	8.14 ± 0.025	8.22 ± 0.032	0.12 ± 0.011	0.07 ± 0.005
Firsov	109.7°E, 5.84°N	HS	8.12 ± 0.018	8.18 ± 0.018	0.15 ± 0.009	0.10 ± 0.007
Marginis Highlands	95°E, 20.5°N	HS	8.14 ± 0.021	8.20 ± 0.018	0.13 ± 0.013	0.09 ± 0.006
Ingenii Highlands	161°E, 34.5°S	HS	8.16 ± 0.035	8.25 ± 0.027	0.11 ± 0.016	0.07 ± 0.009
Airy	3.23°E, 17.88° S	HS	8.12 ± 0.024	8.19 ± 0.020	0.14 ± 0.009	0.09 ± 0.006
Gerasimovich	123.5°W, 23°S	HS	8.11 ± 0.023	8.17 ± 0.024	0.20 ± 0.009	0.16 ± 0.007
Descartes	16.05°E, 10.7° S	HS	8.09 ± 0.027	8.17 ± 0.022	0.16 ± 0.022	0.11 ± 0.011
Kepler	321.9° E, 8.1°N	MC	8.18 ± 0.048	8.28 ± 0.037	0.10 ± 0.005	0.06 ± 0.005
Kepler A	323.8° E, 7.1°N	MC	8.17 ± 0.025	8.28 ± 0.037	0.10 ± 0.005	0.06 ± 0.005
Unnamed K	4.6° E, 35.8°S	MC	8.12 ± 0.016	8.26 ± 0.022	0.11 ± 0.005	0.06 ± 0.002
Unnamed E	4.7° E, 36.8°S	MC	8.07 ± 0.017	8.26 ± 0.022	0.12 ± 0.005	0.06 ± 0.002
Gambart A	341.2° E, 0.96°N	MC	8.13 ± 0.058	8.25 ± 0.034	0.10 ± 0.009	0.07 ± 0.004
Messier	47.6° E, 1.9°S	MC	8.25 ± 0.033	8.29 ± 0.025	0.07 ± 0.006	0.05 ± 0.002
Dionysius	17.2° E, 2.7°N	MC	8.15 ± 0.020	8.25 ± 0.042	0.10 ± 0.007	0.06 ± 0.004
King	120.4°E, 4.9°N	HC	8.09 ± 0.019	8.23 ± 0.019	0.18 ± 0.012	0.09 ± 0.008
Necho	123.2°E, 5°S	HC	8.09 ± 0.019	8.23 ± 0.019	0.17 ± 0.012	0.09 ± 0.008
Pierazzo	259.7°E, 3.3°N	HC	8.06 ± 0.028	8.16 ± 0.018	0.20 ± 0.009	0.12 ± 0.006
Grigg E	125.68°W,13.51°N	HC	8.04 ± 0.028	8.14 ± 0.031	0.19 ± 0.011	0.12 ± 0.007
Byrgius A	296.1°E, 24.5°S	HC	8.05 ± 0.021	8.16 ± 0.031	0.17 ± 0.013	0.11 ± 0.015
Giordano Bruno	102.8°E, 35.9°N	HC	8.03 ± 0.044	8.14 ± 0.024	0.21 ± 0.019	0.12 ± 0.011
Glushko	77.8°W, 5.11°N	HC	8.09 ± 0.028	8.25 ± 0.033	0.14 ± 0.011	0.06 ± 0.005
Unnamed Crater	80°W, 8.9°N	HC	8.06 ± 0.017	8.27 ± 0.018	0.11 ± 0.018	0.07 ± 0.004
Mandel'shtam F	166.1°E,5.1°N	HC	8.04 ± 0.041	8.15 ± 0.022	0.20 ± 0.024	0.12 ± 0.007
Tharp	145.6°E, 30.5°S	HC	8.07 ± 0.025	8.19 ± 0.20	0.17 ± 0.008	0.08 ± 0.004

important to account and correct for them to accurately analyze the data from upcoming and ongoing missions such as Lunar Trailblazer (Ehlmann et al., 2021), OSIRIS-REx (Lauretta et al., 2019) and BepiColombo (Hiesinger and Helbert, 2010).

In this study, we used LRO Diviner data to 1) better understand the effect of space weathering on the CF position in the TIR regime, 2) determine the CF position variation for lunar mare and highlands compositions with respect to visible albedo and optical maturity, and 3) discern the surface space weathering variation of a surface in terms of particle size and iron content.

2. Selection of sites

Greenhagen et al. (2010) noted the influence of space weathering on Diviner CF positions, with the CF appearing to shift to longer wavelengths for mature surfaces compared to younger surfaces such as the crater rays of Tycho. The effects of space weathering on Diviner data were further explored by Glotch et al. (2015) and Lucey et al. (2017; 2021). To study the variation in CF and albedo due to space weathering and the role of particle size and initial iron content in the regolith, we carried out a detailed investigation of two kinds of relatively fresh surfaces on the Moon: 1) lunar swirls and 2) rayed craters (Fig. 1).

2.1. Lunar swirls

Lunar swirls are enigmatic, curvilinear features on the lunar surface characterized by high albedo, low optical maturity, and unusual photometric properties (Hood and Williams, 1989; Blewett et al., 2011; Garrick-Bethell et al., 2011; Hemingway and Garrick-Bethell, 2012; Denevi et al., 2014, 2016; Glotch et al., 2015; Hemingway and Tikoo, 2018). Some of these swirls cause excessive forward scattering of UV and visible light, more so than crater rays (Denevi et al., 2014, 2016). These features are globally distributed on the Moon with no regard for the topography and are associated with remnant magnetic fields on the lunar surface. However, the correlation between magnetic fields and lunar swirls is not 1:1 and not all magnetic anomalies on the Moon display swirls (Denevi et al., 2016; Robinson et al., 2010). Four potential mechanisms for lunar swirls have been proposed: 1) cometary impact (Schultz and Srnka, 1980; Starukhina and Shkuratov, 2004; Bruck Syal and Schultz, 2015), 2) solar wind shielding (Hood and Schubert, 1980; Hood and Williams, 1989; Glotch et al., 2015), 3) electrostatic levitation and transport of dust (Garrick-Bethell et al., 2011; Hemingway and Garrick-Bethell, 2012), and 4) magnetic sorting of dust (Pieters et al., 2014). Several studies (e.g., Pieters and Noble, 2016; Hess et al., 2020) suggest that these swirls are less mature than the surrounding regions. In fact, they do display the presence of microphase iron on the on-swirl regions (Trang and Lucey, 2019). This could be attributed to the fact that though the solar wind is deflected by the magnetic field present at swirls, micrometeoroids still hit the surface, leading to a lesser degree of space weathering on these surfaces. Hess et al. (2020) modeled the off-swirl region VNIR spectra via a combination of space weathered and/or compacted on-swirl VNIR spectra. They suggest that the swirls are less space weathered and could be more compact and fine-grained at places (Garrick-Bethell et al., 2011; Hess et al., 2020). The TIR study of lunar swirls by Glotch et al. (2015) suggested that CF shifts to shorter wavelengths for on-swirl regions compared to off-swirl regions but no distinct fine-grained layer was observed based on night-time cooling trends in Diviner temperature data.

2.2. Rayed craters

Impact cratering is one of the most widespread and dominant processes in our Solar System. Crater rays were first noted in telescopic observations by Gold (1955). Using stratigraphic relationships,

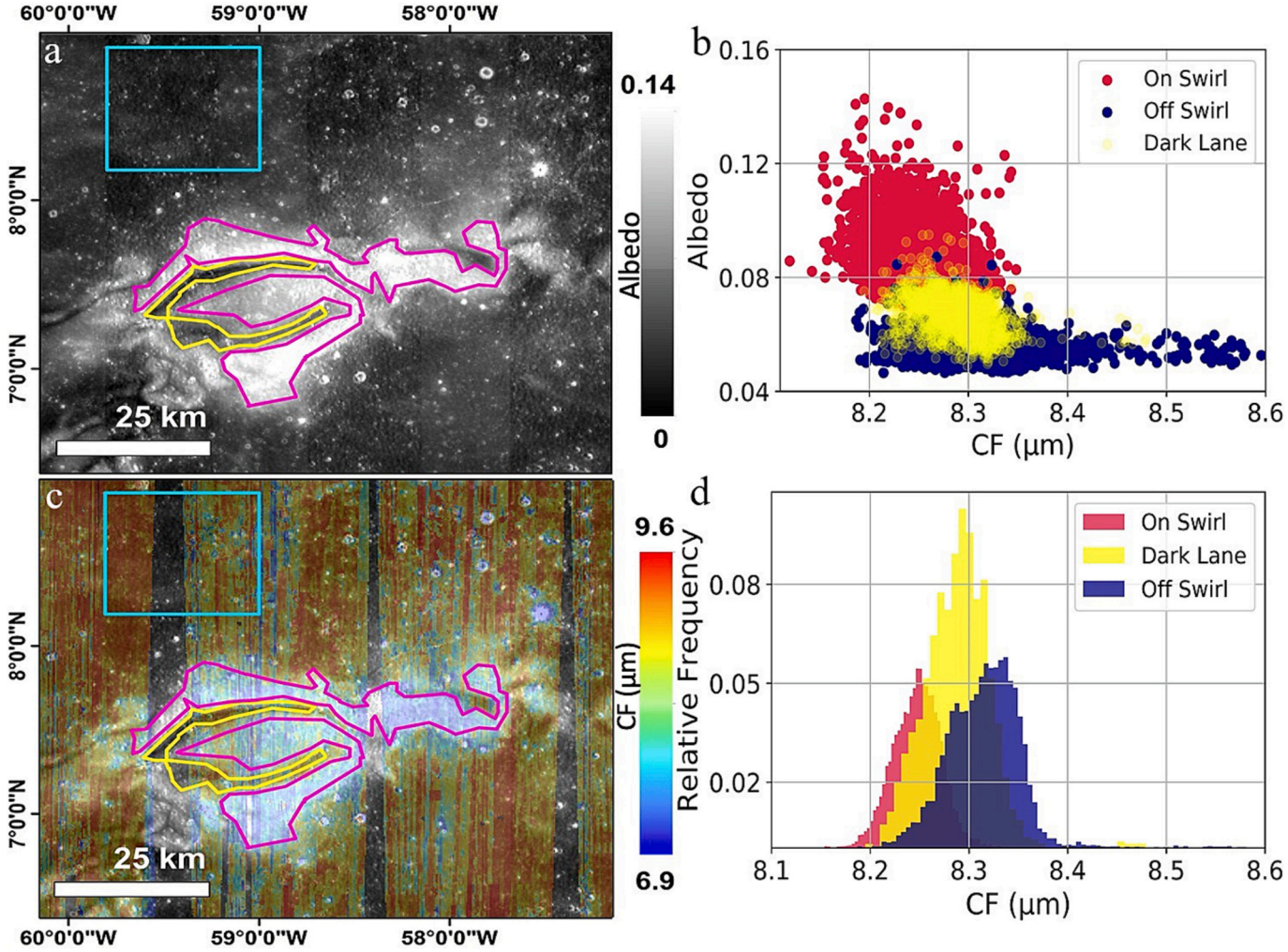

Fig. 2. a) Kaguya albedo map with overlayed outlines of the sampled sites. On-swirl region is outlined in pink, the dark lanes are outlined in yellow, and off-swirl region is outlined in blue. b) Scatterplot of albedo vs CF of the three regions c) CF image of the Reiner Gamma region overlaid on the Kaguya albedo map d)Histogram displaying the CF distributions in the on-swirl, dark lane and off-swirl regions. Relative frequency is the percentage of pixels with those CF values. (For interpretation of the references to colour in this figure legend, the reader is referred to the web version of this article.)

Shoemaker and Hackman (1962) suggested that rayed craters are among the youngest features on the Moon and that upon impact the ejected material was deposited around the craters following a ballistic trajectory as rays. With time, due to space weathering, these rays mature and darken, thus the craters with distinct visible ejecta patterns must have formed recently in the Copernican era (~ 800 Ma; Gold, 1955; Neumann et al., 2015). Grier et al. (2001) used optical maturity of the crater rays and their distribution from the crater rims for relative dating of lunar surfaces. The optical maturity (OMAT, Lucey et al., 2000a, 2000b)) values are a proxy to quantify the maturity and changes in optical properties of the lunar soil (Lucey et al., 2000a, 2000b), with higher OMAT values indicating lower maturity of regolith and vice-versa. The rayed craters display a systematic decrease in OMAT values away from the crater rim (Grier et al., 2001). The asymmetry in number of rayed craters on the mare versus highlands surfaces exists as a result of the ray detectability being lower in the mare region due to the composition as the process of space weathering-induced darkening is faster for mare regions (Werner and Medvedev, 2010). Crater rays stand out in Diviner CF maps indicating that space weathering also affects the TIR measurements (Lucey et al., 2017; 2021).

Crater rays can also be used to investigate particle size variations in the lunar regolith. Bart and Melosh (2010) carried out a detailed study of boulder size distributions around lunar craters and found that the larger boulders ejected during crater excavation preferentially lie closer to the crater rim. The smaller (> 0.25 m) boulders are widespread while the larger boulders decrease in abundance moving away from the crater rim. The size of boulders is important because large boulders take longer to break down compared to smaller ones. We have used this to investigate the fraction of the Diviner spatial footprint covered by rocks smaller than those measured by Diviner rock abundance (~1 m diameter) but larger than typical regolith fines and its effect on the CF position.

2.3. *Properties of lunar swirls and rayed craters*

The proposed formation models for lunar swirls generally suggest that the lunar swirls are old and host relatively less optically mature surfaces with higher albedos than the surrounding background regolith material and dark lanes in both mare and highlands regions. These surfaces are also fine grained and lack any blocky materials or rocks (Garrick-Bethell et al., 2011; Hess et al., 2020). The rayed craters, on the other hand, are widespread across the lunar surface, host high rock abundance near the crater rims, display high thermal inertia throughout the rays, and exhibit immature rays superimposed on the mature space weathered background regolith (Grier et al., 2001; Bart and Melosh, 2010; Hayne et al., 2017). Both these surfaces provide unique opportunities with varying particle size and rock abundance to investigate the effects of space weathering. Essentially, each site hosts similar bulk silicate compositions, but different particle size distributions and levels

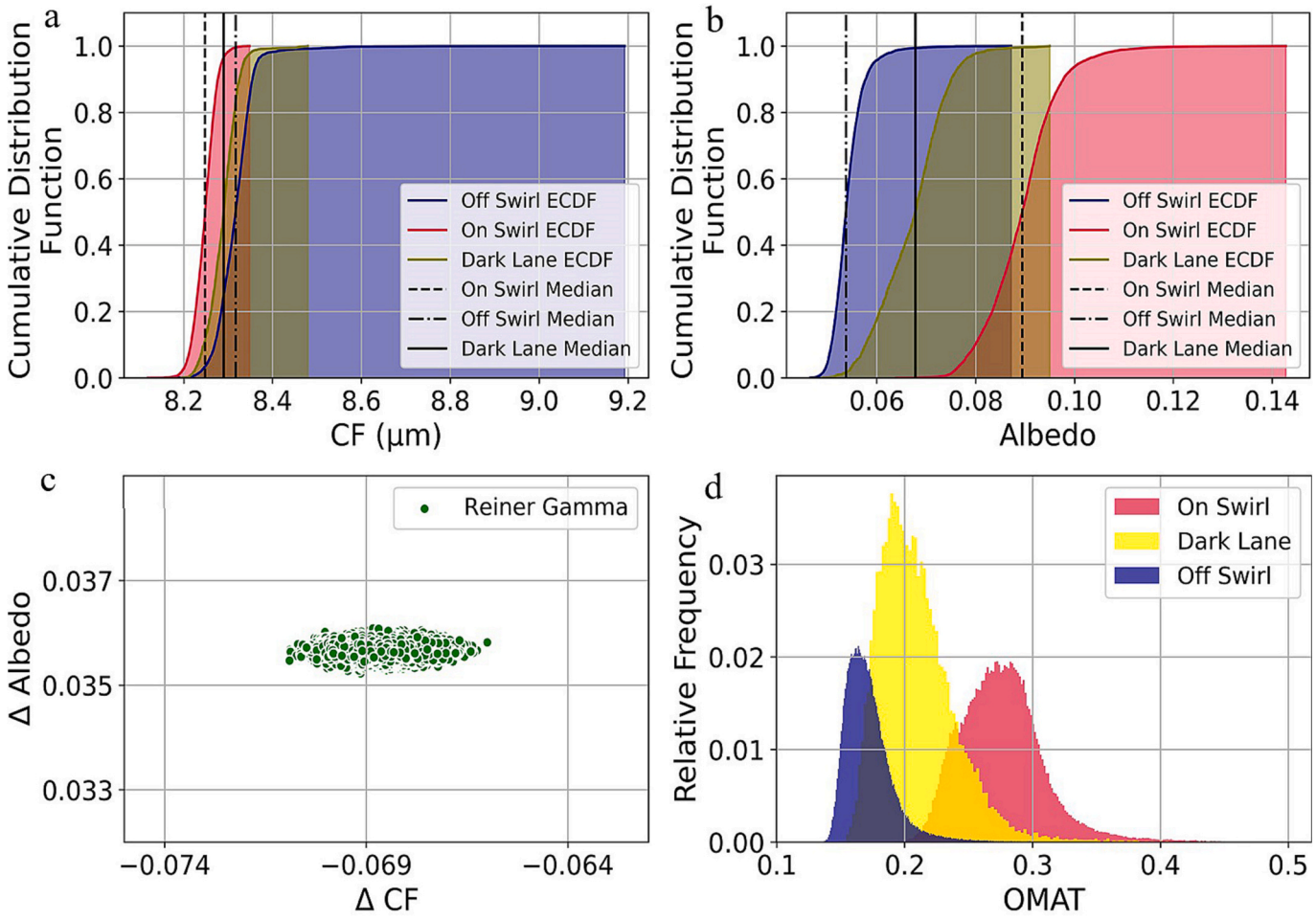

Fig. 3. a) On-swirl and off-swirl empirical cumulative distribution functions of CF b) On-swirl and off-swirl empirical cumulative distribution function of albedo c) On-swirl and off-swirl CF and albedo difference scatterplot of the Reiner Gamma region d) Histogram displaying the optical maturity (OMAT) distributions in the on-swirl, dark lane and off-swirl regions.

of space weathering undergone by the surfaces. In this study, we have selected 29 such locations (Table 1) across the lunar surface comprised of younger rayed craters and swirls located both in the highlands and mare, to carry out a detailed study to understand the effect of space weathering on CF with respect to fraction of boulders, particle sizes and iron content (maria Vs highlands) (Table 1; Fig. 1).

3. Datasets and methods

CF positions were calculated from emissivity data from Diviner channels 3, 4 and 5 corresponding to 7.55–8.05 μm, 8.1–8.4 μm, and 8.38–8.68 μm (Paige et al., 2010) using the methods of Greenhagen et al. (2010). We selected daytime (local time 10:00 am to 2:00 pm) orbital data from 2009 to 2020 to have a comprehensive set of CF maps for all the sites and to minimize the effects of solar incidence angle on the estimated CF position. We have used the CF values photometrically corrected in agreement with Greenhagen et al. (2011) binned at 128/256 pixels per degree (PPD), which corresponds to ~250/~125 m/px at the equator. Note: At 256 ppd., the Diviner data are slightly over-sampled. We also used level 3 Kaguya Multiband Imager (MI) Band 2 reflectance data (750 nm) with spatial resolutions of 128 or 256 ppd. to characterize the visible albedos of our study sites. The uncertainty for CF measurement is ~0.002 μm (Paige et al., 2010). The measurement of pixel-to-pixel sensitivity of Kaguya calibrated reflectance data within a band is <2% (Ohtake et al., 2008). The CF and Kaguya reflectance datasets were georeferenced using the DaVinci and ENVI software packages. A region of interest (ROI) for each feature was selected manually following albedo trends for swirls and rays. Furthermore, we converted them to shapefiles of the selected regions and overlayed them using ArcMap. Any potential bias in the ROI sampling and analysis has been removed via the statistical analysis detailed below. We selected the rayed craters from the crater catalogue of Grier et al. (2001) and following that individually carried out detailed literature review on the selected craters and removed the craters suspected to have excavated different lithology using existing VNIR and TIR data. We have also selected the areas right around the craters to minimize the difference between the excavated and surrounding material. We have carefully selected the sites without any anomalous composition; thus, it is reasonable to presume that the bulk composition of the on-site and off-site regions at each feature are similar.

The H-parameter values calculated from Diviner temperature data are an indicator of thermal conductivity and density of regolith with in the uppermost 10s cm regolith depth. The lower the H-parameter value, higher density and thermal conductivity are found at shallower depths and vice versa (Hayne et al., 2017). H-parameter is also used as a proxy for thermal inertia and is inversely related to it. Thermal inertia is the ability of a material to conduct and store heat. Thermal inertia of coarse grains and rocks is higher than fine grained regolith. Thus, the H-parameter of coarse-grained regolith and rocks is lower than finer-grained regolith. In addition, the H-parameter of fluffier porous regolith (such as lunar cold spots) is higher compared to compact material (Hayne et al., 2017). The 128 ppd. H-parameter map from Hayne et al.

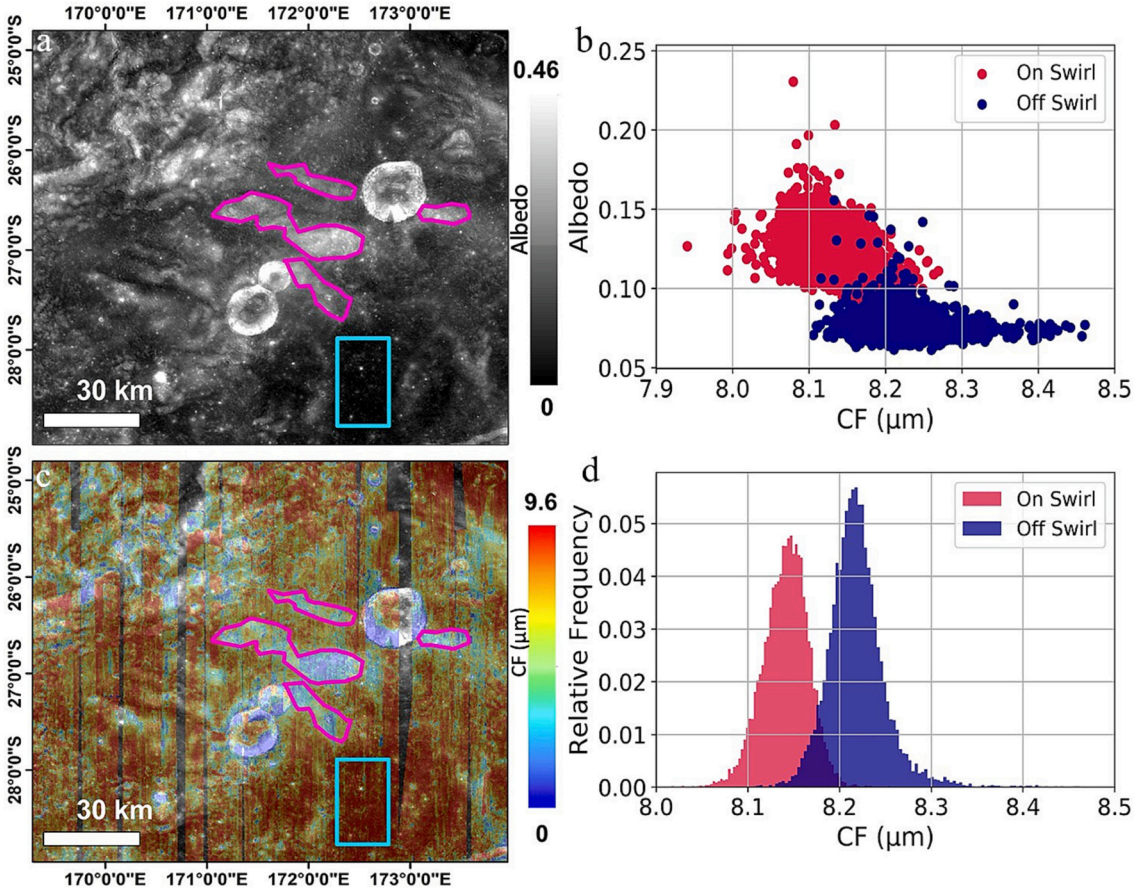

Fig. 4. a) Kaguya albedo map with overlayed sampled sites from on-swirl region (outlined in pink) and off-swirl region (outlined in blue). b) Scatterplot of albedo vs CF of the on-swirl and off-swirl locations c) CF image of the Van de Graaff crater overlayed on a Kaguya albedo map d) Histogram displaying the CF distributions in the on-swirl and off-swirl regions. (For interpretation of the references to colour in this figure legend, the reader is referred to the web version of this article.)

(2017) with uncertainty of <6% is used to investigate the particle size and rock abundance variation between craters and swirls.

The magnetic field data used in this study has been adopted from Table 1 and the figures of Blewett et al. (2011). These data were derived from the total field strength from the Lunar Prospector magnetometer at 30 km altitude by Blewett et al. (2011) via location and contour comparison from Table 1 and Figs. 1–6 respectively in that paper.

3.1. Selection of ROIs

The ROIs were manually selected for both the on-swirl/ray, off -swirl/ray and dark lane of the swirls using albedo and CF maps. No general cutoff value for albedo was used because the albedo varies with location due to varying levels of space weathering. For instance, Kepler and Kepler A crater ROIs have different on-ray albedo values compared to the off-ray regions as they have undergone different amount of space weathering. A cut-off albedo value would also prevent us from capturing the curved features within lunar swirls and decrease our sample size. To make sure we account for this, we have used the median OMAT values of the ROIs for comparison and analysis in our discussion section (Table A2 in Appendix). We have also been very careful to prevent any bias due to inclusion of the high-albedo pixels within off-swirl/ray ROIs due to the presence of young impact craters and low-albedo pixels within on-swirl/ray ROIs due to pixels from dark lane or imperfect rays with background.

First to avoid the influence of such pixels, we use the median rather than the mean of the ROIs in our comparative analysis. Median values are not influenced by any outliers (in this case the high albedo and low albedo pixels). Following that we have treated the ROIs as a sample instead of a whole population, i.e., we have taken 10^5 combinations of the pixel values of each ROI and calculated their difference. If the outliers were present in large numbers quantitatively, they would heavily skew the median and thus we would get a large range of differences. We do not observe a large range of difference (Table A1 in Appendix), thus once again confirming that these outliers do not affect our analysis or interpretation in any manner.

In addition to the previous steps, we also ran a non-parametric hypothesis test with 5% significance ($p < 0.05$) to confirm that the different ROIs within a site that we are investigating are different (See section Appendix section 1 for detailed explanation). The delta CF has been estimated by subtracting off-swirl/ray regions from the on-swirl/ray regions.

Overall, we have actively taken three steps (choosing median; bootstrapping; hypothesis testing) to avoid any bias introduced by foreseen (ROI shapefiles) and unforeseen activities, thus we can confidently say that the analysis done using the albedo and CF values is statistically robust with minimal bias, if any. We have used statistical bins instead of manually deciding on a number to avoid binning bias (which can lead to skewness and misinterpretation among other things) for histograms of the CF and albedo values.

4. Results

4.1. Swirls

We investigated several mare swirls, including Reiner Gamma located in Oceanus Procellarum, and others in Mare Ingenii, Mare Marginis, Hopmann, Rimae Sirlsalis and Moscoviense basin.

Reiner Gamma is a tadpole-shaped lunar swirl present on the

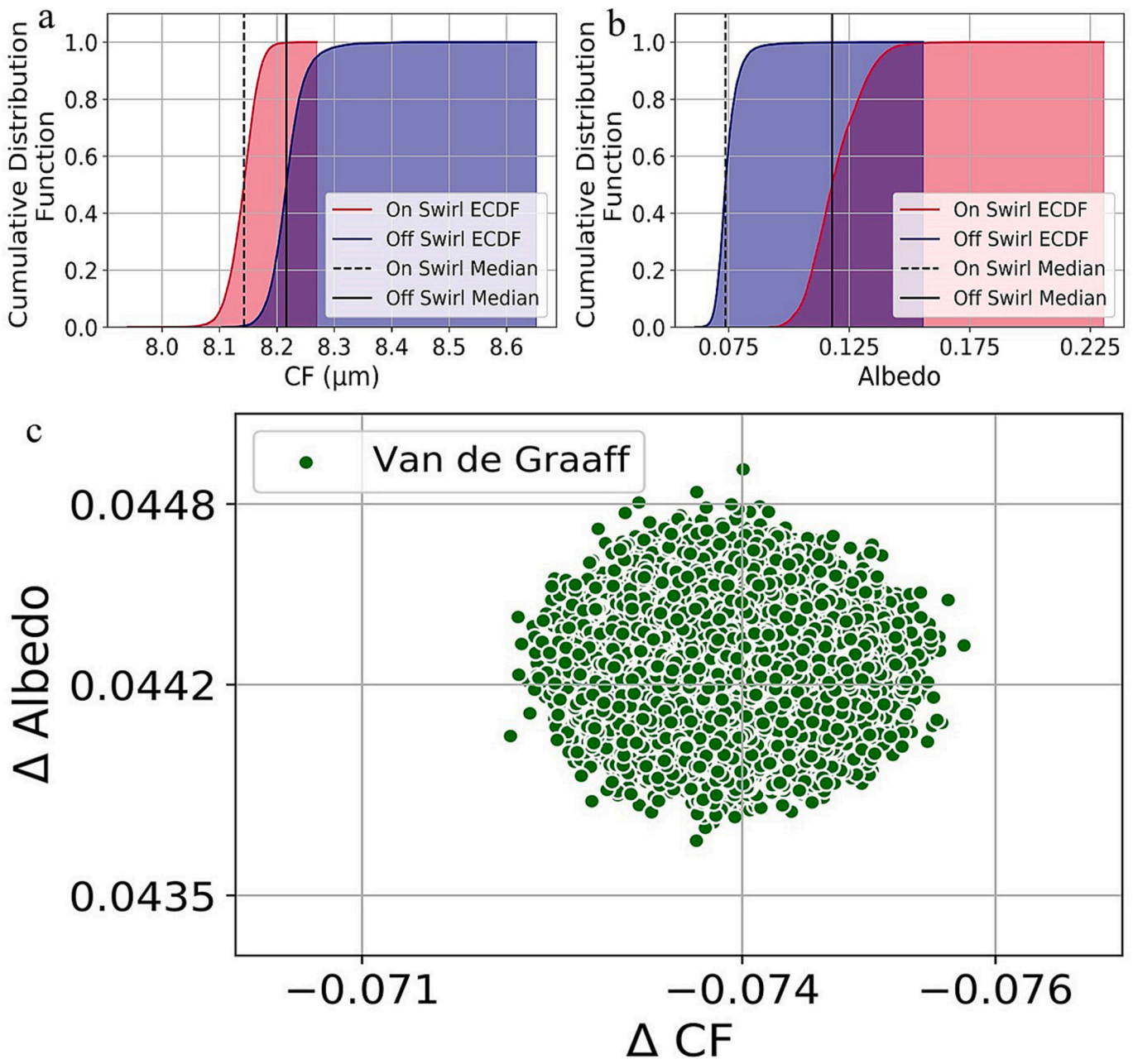

Fig. 5. a) On-swirl and off-swirl empirical cumulative distribution function (CDF) of CF b) On-swirl and off-swirl empirical cumulative distribution function (CDF) of albedo c) On-swirl and off-swirl CF and albedo difference scatterplot of Van de Graaff region.

nearside of the Moon (Fig. 2a, c). The on-swirl region has a median visible albedo of 0.09 (as measured by the Kaguya Multispectral Imager (MI) at 750 nm), while the dark lane and off-swirl regions have median albedos of 0.06 and 0.05 respectively. The CF position of the high albedo swirl region is at shorter wavelength relative to the dark lanes and off-swirl (mare), with a median of 8.25 μm while the dark lane and off-swirl regions have median values of 8.28 μm and 8.31 μm respectively. The scatterplot in Fig. 2b shows that the on-swirl region has a higher albedo and shorter wavelength CF position than the dark lanes and off-swirl regolith. The histogram in Fig. 2d shows that the dark lane CF position overlaps both the on-swirl and off-swirl regions. We also observe some overlap between the on-swirl and off-swirl region.

The difference in CF between the on-swirl and off-swirl regions is -0.07^{+}_{-} 0.0005 μm (Fig. 3c) and between the on-swirl and dark lane is -0.04^{+}_{-} 0.0009 μm. The albedo difference between on-swirl and off-swirl region is 0.04^{+}_{-} 9.72 e^{-05} and on-swirl regions to dark lane is 0.02^{+}_{-} 0.0002 μm (Fig. 3c). The CF difference between the dark lane and off-swirl region is -0.03^{+}_{-} 0.0009 μm and the albedo difference is 0.01^{+}_{-} 0.0002 μm. The range of CF and albedo median differences being below the data sensitivity indicate that assuming one median value to be representative of the sample is statistically appropriate to proceed with the analysis.

We have also plotted their empirical cumulative distribution functions (ECDF) for the same array size as the observed one with the initial values (Fig. 3a, b). The ECDF plots indicate that CF values are less scattered since the slope of the CDFs are steep while more scattered in case of albedo as seen with the relatively gentle slopes (Fig. 3a, b). We carried out a KS test on three set of samples: 1) on-swirl and dark lane 2) on-swirl and off-swirl region, and 3) dark lane and off-swirl region and calculated the D-statistic values to investigate if the dark lane and on/off-swirl regions belong to the same distribution since their CF values seem to overlap in the histogram (Fig. 2d). The D-statistic has to be

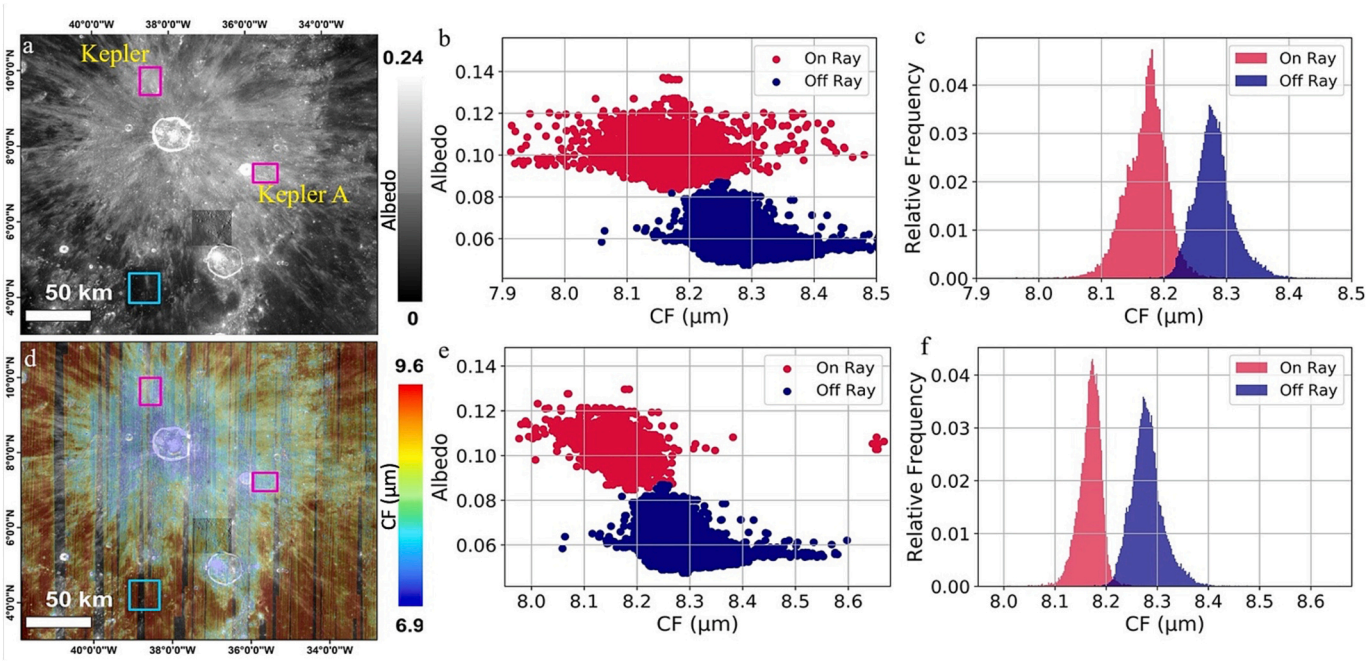

Fig. 6. a) Kaguya albedo map with overlayed sampled sites from the on-ray region outlined in pink and the off-ray region outlined in blue. b) Scatterplot of albedo vs CF for the on-ray and off-ray regions of Kepler c) Histogram displaying the CF distributions for the on-ray and off-ray regions of Kepler d) CF image of the Kepler and Kepler A crater overlayed on a Kaguya albedo map e)Scatterplot of albedo vs CF for the on-ray and off-ray regions of Kepler A f) Histogram displaying the CF distributions for the on-ray and off-ray regions of Kepler A. (For interpretation of the references to colour in this figure legend, the reader is referred to the web version of this article.)

higher than the critical value of the two samples and the *p*-value should be lower than the assumed value of the α coefficient for them to have different distributions, which we see here. The critical values for the three sets is much smaller than their D-statistics (Table A1 in Appendix). The *p*-values for all the sets were 0. The values of D-statistics being higher than their respective critical values for all the three sets indicate that though the dark lane values overlay both on and off-swirl regions, they all have different distributions. This leads us to reject the null hypothesis and thus the variation in CF distribution that we observe between the on-swirl region, dark lanes and off-swirl regions is real and not arbitrary. The OMAT values plotted as a histogram of the on-swirl, dark lane and off-swirl regions show that the on-swirl regions are least mature, followed by dark lane and then the off-swirl regions (Fig. 3d). We do observe an overlap between the OMAT values of all the three regions as well. This variation in OMAT, albedo and CF values might mean that the dark lanes represent the transition from on-swirl to off-swirl regions on the spectrum of space weathering.

The median and statistical test values for all swirls are given in Table A1 in Appendix. The OMAT values are available in Table A2 in Appendix. We note that an opposite trend is observed in the cases of the swirls in Sirsalis and Moscoviense where the CFs of on-swirl regions are higher than the off-swirl region. We have not included Mare Moscoviense and Sirsalis swirl in the final plot of delta CF vs delta albedo despite rejecting the null hypothesis in both the cases due to two reasons: 1) The Diviner maps are heavily striped in both these regions despite using tighter constraints of incidence angles, time of day, activity flag etc. The stripes that persist through the normalization to equatorial noon imply that the correction is not doing a good job for those areas which is fairly typical for darker mare and is most likely caused by relatively smaller populations of these compositions in the photometric fits (Greenhagen et al., 2010, 2011). 2) The striped data is apparent in the statistical test where the D-statistic for CF samples of both the swirls is very close to 0 instead of 1, indicating that while the on-swirl regions are statistically separable from off-swirl regions, this difference is very small.

In the highlands, we examined swirls within Van de Graaff crater, Firsov crater, Marginis highlands, Ingenii highlands, Gerasimovich crater, and near Airy and Descartes craters. The swirls in Van de Graaff lie on the crater floor and appear in a wavy pattern with high albedo compared to the surroundings (Fig. 4a, c). In the scatterplot, we see that the on-swirl and off-swirl CF values plot in two distinct clusters (Fig. 4b) with some overlap and we observe a similar trend in the histogram (Fig. 4d). The ECDF plots indicate that CF values are less scattered since the slope of the CDFs are steep while more scattered in case of albedo for on-swirl region as seen with the relatively gentle slopes (Fig. 5a, b).

The median albedo of the on-swirl region is 0.12 and the median CF is 8.14 μm. The median off-swirl albedo and CF values are 0.07 and 8.22 μm, respectively (Fig. 5a, b). The CF difference between the on-swirl and off-swirl regions is -0.07^{+}_{-} 0.0003 μm and the albedo difference is 0.04^{+}_{-} 0.0001 (Fig. 5c). As shown in Table A1 in Appendix, the D-statistics are larger than the critical values and *p*-value smaller than the significance level, leading to rejection of the null hypothesis.

The median and statistical values of all the other highlands swirls are given in Table 1, Table A1 and Table A2 in Appendix.

4.2. Copernican craters

We examined 7 craters with bright rays located in mare regions. These include Kepler, Kepler A, Gambart A, Messier, Dionysius and two unnamed craters. Craters Kepler and Kepler A have diameters of 29 km and 11 km, respectively, and display bright, radial rays (Fig. 6.a, d). Kepler A is located on the ejecta of Kepler with relatively higher albedo than the surroundings and makes a useful point of comparison to inspect the increasing effects of space weathering within regions with similar bulk composition. Due to the close proximities of the two craters, we have taken a common background mature mare region to compare to both of their crater rays. The median CFs of the on-ray regions of Kepler and Kepler A are both 8.17 μm, respectively, while the CF of the background mare region is 8.27 μm. The median albedo is 0.09 for Kepler, 0.10 for Kepler A, and 0.05 for the mature mare background. The

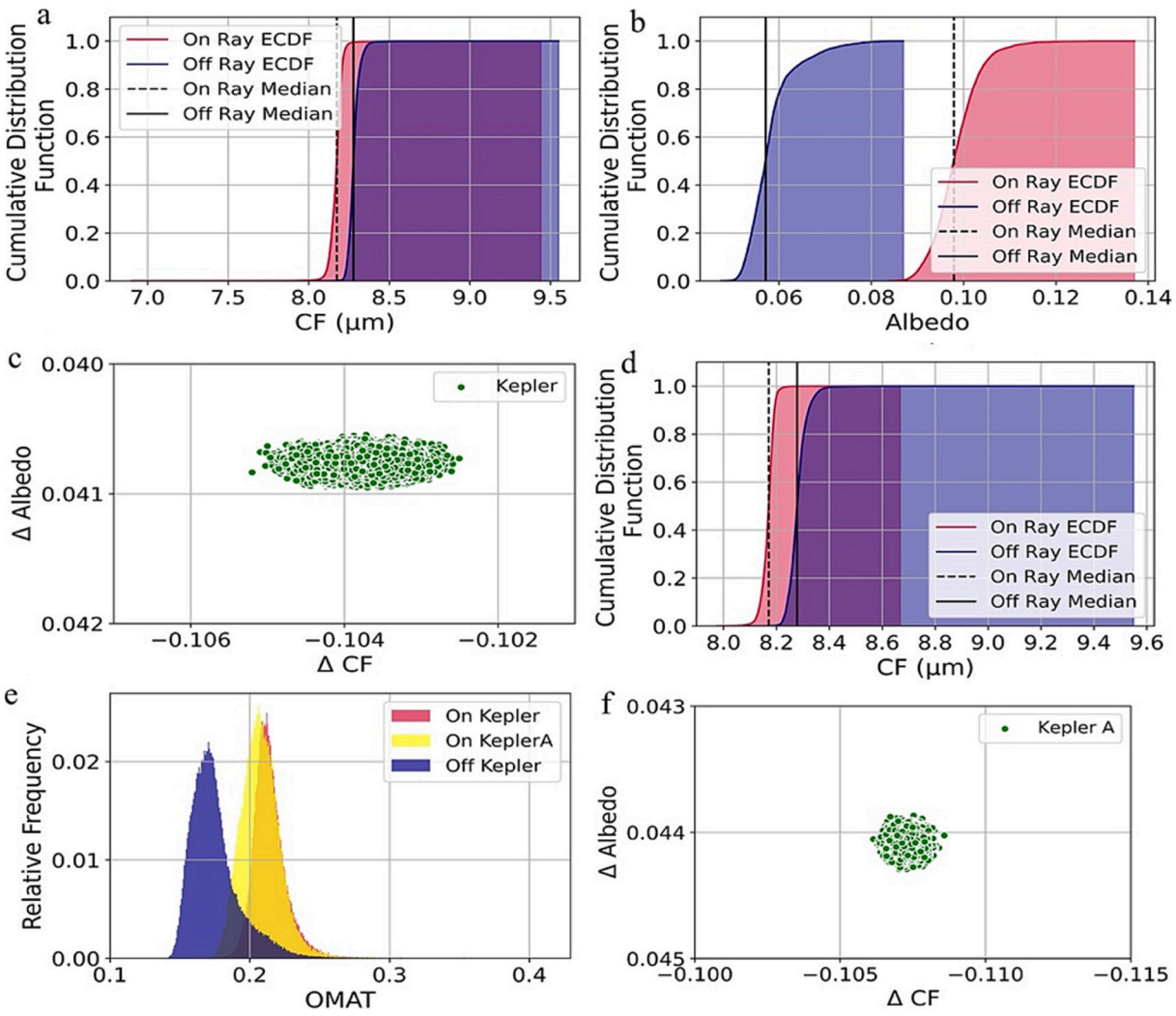

Fig. 7. a) On and off-ray ECDF for CF of Kepler b) On and off-ray ECDF for albedo of Kepler. c) Scatterplot of albedo vs CF differences for the on-ray and off-ray regions of Kepler d) On and off-ray ECDF for CF of Kepler A e)Histogram displaying the OMAT distributions for the off-ray and on-ray regions of Kepler and Kepler A f) Scatterplot of albedo vs CF differences for the on-ray and off-ray regions of Kepler A.

scatterplot for both the craters demonstrates that the off-ray and on-ray regions plot separately in two clusters (Fig. 6.b, e) with some overlap with off-ray regions. We observe a similar trend in the histogram (Fig. 6. c, f) with some overlap for Kepler and very little overlap between the on and off ray regions for Kepler A. The difference in CF between Kepler and the background is -0.10^{+}_{-} 0.0002 μm, while the difference between Kepler A and the background is -0.11^{+}_{-} 0.0002 μm. The albedo differences are 0.04^{+}_{-} 5.15e^{-05} and 0.04^{+}_{-} 4.79e^{-05}, respectively (Fig. 7c, f).

The ECDFs of CF for Kepler and Kepler A have steep slopes which indicates that the data points for both areas are clustered together without much spread except the outliers (Fig. 7a, d). However, the albedo ECDF indicates that both the regions have relatively larger spread in the values because of their relatively gentler slopes (Fig. 7b). The OMAT histogram of the three regions shows that the on-ray region of Kepler is least mature, followed by Kepler A and further by off-ray region (Fig. 7e). The D-statistics for both craters are higher than the critical value and the *p*-values are lower than α, thus leading us to reject the null hypothesis (Table A1 in Appendix). We observe a higher median albedo and lower median CF for Kepler A rays compared to Kepler which is in contrast to their maturity where Kepler A is more mature than the Kepler. The D-statistics of the CF samples are also higher for Kepler A than Kepler, indicating the difference between Kepler A rays and background is slightly higher than that of Kepler rays and background. The median values for other mare craters and the statistical values are given in Table 1 and Table A1 in Appendix in detail.

In the highlands, we carried out a similar comparison on 10 craters, including King, Necho, Pierazzo, Grigg E, Byrgius A, Giordano Bruno, Glushko, Mandel'shtam F, Tharp, and three unnamed craters.

Giordano Bruno is a 21 km crater located at 102.8° E, 35.9° N associated with a bright rayed ejecta deposit (Fig. 8a, c) and impact melt deposits on the southern rim. In choosing our on-ray ROI, we have avoided any regions with melt deposits that could be compositionally altered. The scatterplot and histogram of the on and off-ray ROI show separate clusters with some overlap (Fig. 8b, d). The median values of albedo for on-ray and off-ray ROI are 0.21 and 0.12 respectively. The median values for on and off-ray CF are 8.03 μm and 8.14 μm respectively. The CF difference between the on-ray and off-ray regions of Giordano Bruno is $-0.11^{+}_{-}0.0005$ μm (Fig. 9c) and the albedo difference is $0.10^{+}_{-}0.0003$. The slopes of ECDFs for the on and off-ray regions are relatively gentle indicating that the values are relatively widespread for both CF and albedo. Based on the D-statistics, critical values and p-values in Table A1 in Appendix, we reject null hypothesis for these regions.

Similar details of other highlands craters are given in Tables 1 and A1.

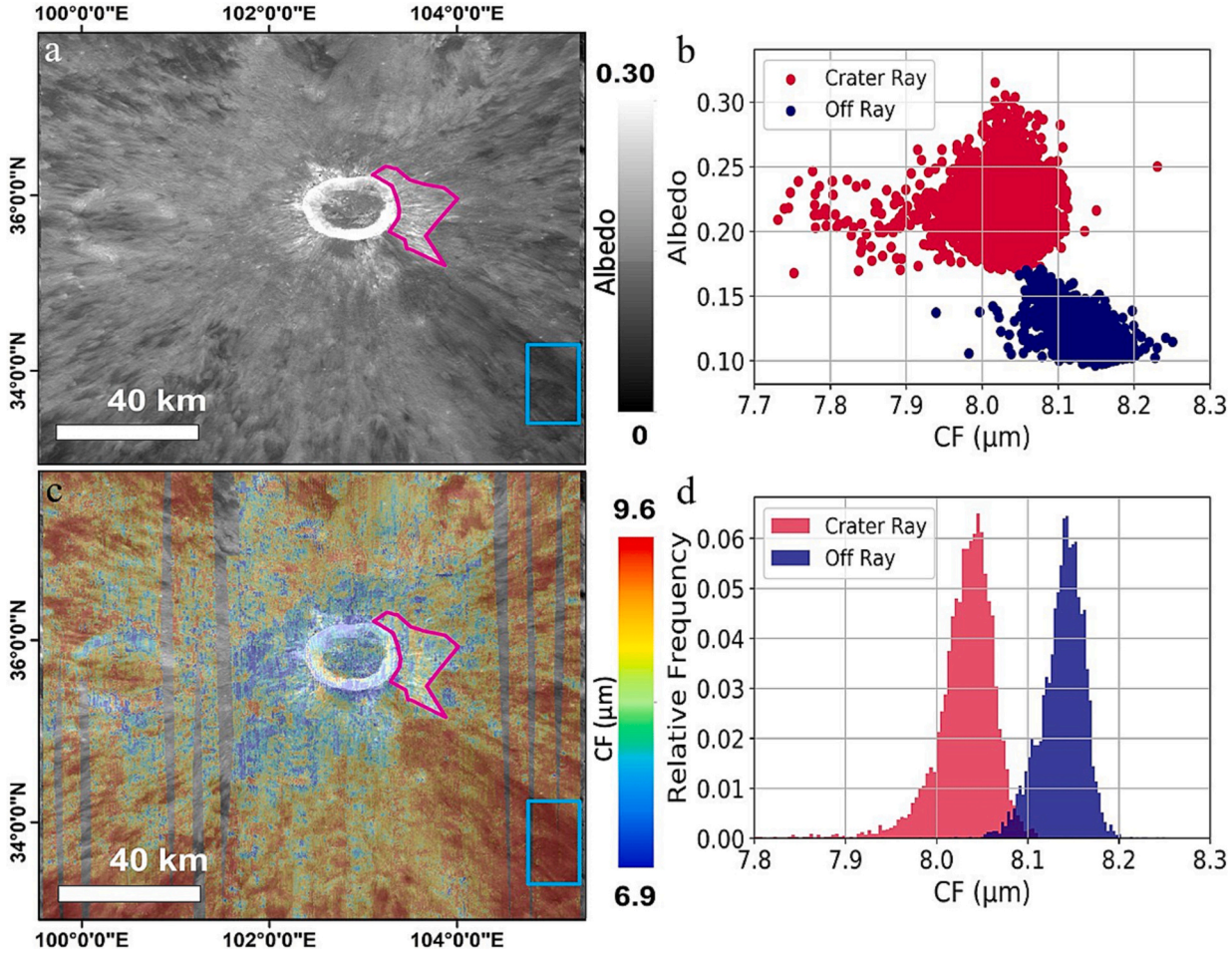

Fig. 8. CF and albedo statistics for Giordano Bruno crater. a) Kaguya albedo map with overlayed sampled sites from the on-ray regions outlined in pink and the off-ray region outlined in blue b) Scatterplot of albedo vs CF for the on- and off-ray regions for King crater c) CF image of Giordano Bruno d) Histogram displaying the CF distributions of the on-ray and off-ray regions of Giordano Bruno. (For interpretation of the references to colour in this figure legend, the reader is referred to the web version of this article.)

4.3. H-parameter and rock abundance

The rock abundance (RA) maps of Bandfield et al. (2011) display the surface area fraction of rocks (~1 m or greater) within a pixel. Most surfaces have RA values between 0 and 0.01 (converted to percentage in Fig. 10b) (Table A2 in the Appendix). We have used the median value of the RA and H-parameter maps overlaying the ROIs to measure the rockiness of the surface. The H-parameter and RA difference have been calculated by subtracting the average value of mare region (0.07 for H-parameter,0.4% for RA taken from Byron et al., 2022) from the ROIs.

We have compared H-parameter and RA variations of on-swirl and on-ray regions among themselves. The RA values of the on-ray regions vary between 0.2% and ~ 8% and on-swirl regions vary between 0.3% and ~ 0.5%. The RA values of the on-swirl regions are lower than the on-ray regions. For swirls, we observe that the RA values are higher for the highland swirls compared to mare swirls. Our observations show that the H-parameter values are mostly higher on the on-swirl regions compared to crater rays.

The H-parameter values of the on-swirl regions vary from ~0.08 m to ~0.09 m and the on-ray regions vary from ~0.05 m to ~0.08 m. On-swirl regions display higher H-parameter values compared to on-ray and average mare regions. The H-parameter values (~ 0.08 m) of the swirls are high, but they are not as fluffy as cold spots (typical H-param >0.1 m) or composed of pyroclastic material (Hess et al., 2020). The H-parameter (mostly greater >0.05 m) values of the rayed regions are also the same as the majority of the lunar surface.

Overall, we observe that the swirls have lower RA and higher H-parameter compared to mare regions and higher H-parameter compared to crater rays.

5. Discussion

Prior to Diviner observations, space weathering was not expected to affect TIR emission measurements. However, the spectral effects of space weathering on TIR measurements (a shift of CF to longer wavelengths and reduction of band contrast) have been observed in several remote sensing and laboratory studies (Glotch et al., 2015; Lucey et al., 2017, 2021; Shirley, 2018; Shirley et al., 2023). The leading hypothesis for these effects is the reduction of visible albedo and associated reduction in thermal gradient, which alters the CF position and reduces observed contrast. Several efforts to produce a global correction for the effects of space weathering on CF have been made (Lucey et al., 2017; Lucey et al., 2021). Here we will describe our observation of CF variation between on-swirl/ray and off-swirl/ray regions as well as between the mare vs highlands and crater ray vs swirls and their relevance to space weathering correction efforts.

5.1. CF variation between on-swirl/ray and off-swirl/ray region

The observed histograms for all the sites (Fig. 2d,4d,6.c,6.f,8d) display some overlap in the ROI distributions both for CF and albedo values. This overlap is higher for swirls than crater rays because the

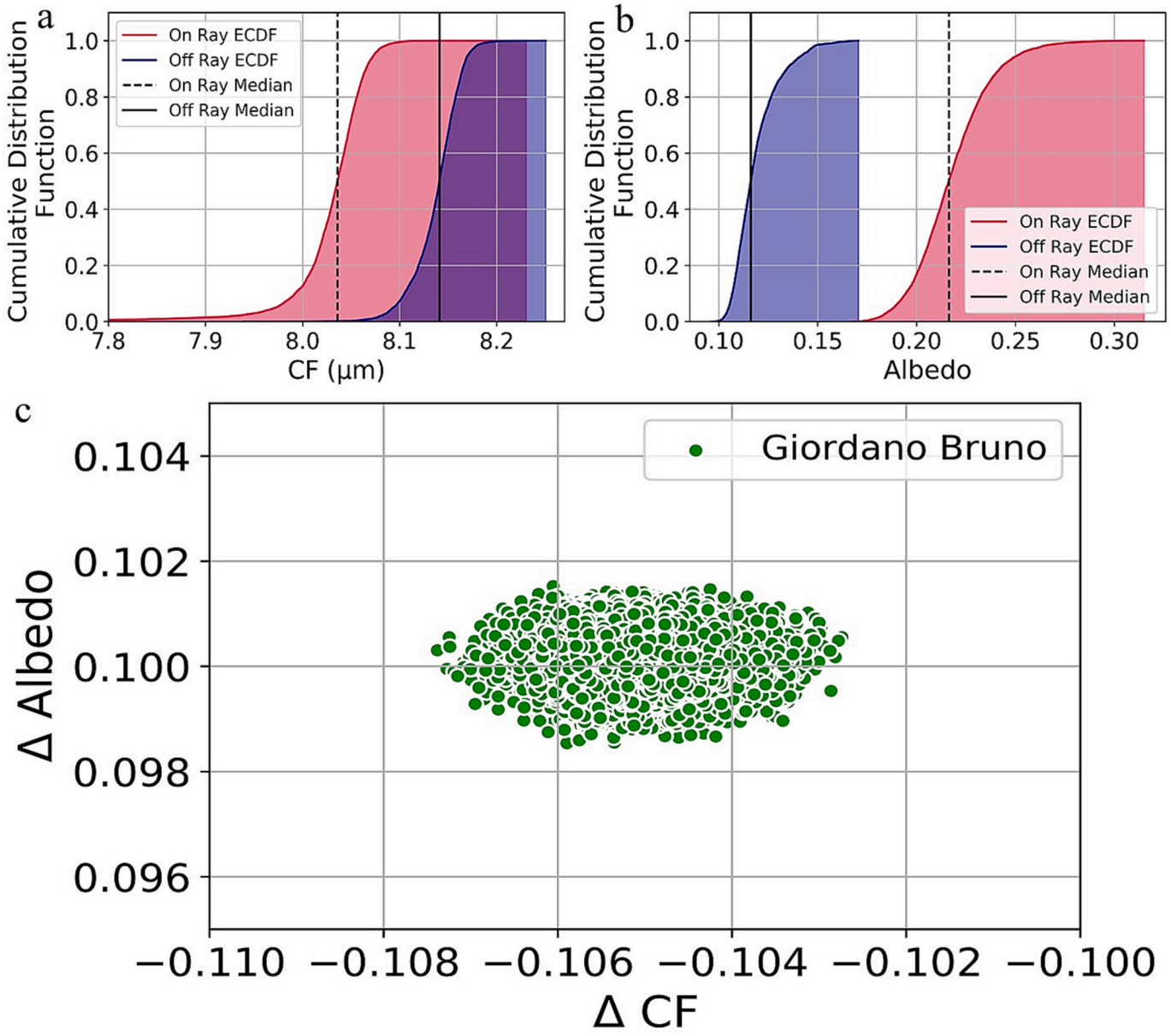

Fig. 9. a) On and off-ray ECDF of CF b) On and off-ray ECDF of albedo c) Scatterplot of albedo vs CF for the on-ray and off-ray regions of Giordano Bruno.

variation in albedo is larger for on-ray and off-ray regions than for on- and off-swirl regions. Also, while selecting crater rays, we were careful to choose regions that were completely covered by the rays with the least amount of the background (off-ray region). Thus, there was a minimal range of common albedo values and the overlap we see is primarily due to a few outlier pixels mostly within the ROIs. This overlap in CF and albedo histograms is higher for swirl regions because as we move away from the central portion of a swirl towards its edges, the albedo decreases gradually but substantially. This decrease in albedo is because even within a swirl the degree of space weathering away from the center (location with maximum magnetic field strength) presumably increases. This phenomenon can also be seen in the histogram for on-swirl OMAT values (Fig. 3d) where even though most of the population lies between on and off-swirl values, there is still a significant overlap between these regions.

In addition, the median values of OMAT and albedo for the swirl dark lanes lie between the on-swirl and off-swirl regions. The CF positions of the dark lanes are at longer wavelengths than the swirls, but at shorter wavelengths than the mature regolith in the background, indicating that these lanes could be intermediate transition zones from immature regolith in lunar swirls to mature regolith in the background. A possible transition zone suggests that the magnetic fields might be close to, but not truly vertical in these regions, resulting in some deflection of the charged particles (Blewett et al., 2011; Garrick-Bethell et al., 2011). It is possible that only a portion of the funneled charged particles make it to the surface, partly slowing down the maturation process instead of making it ultra-mature, as has been previously suggested (Hood and Williams, 1989; Blewett et al., 2011).

5.1.1. *Variation between on-swirl and on-ray regions*

Fig. 10c shows that on-swirl regions have lower RA and higher H-parameter values compared to craters. The variation in CF that we observe between swirls and craters for comparable albedo changes could result from a larger average particle size distribution due to the presence of small rocks (< 1 m but larger than typical regolith fines) mixed with the regolith at the rays. Following Byron et al. (2022), the regions we observe with higher H-parameter (i.e., the swirls) could be interpreted as having a relatively finer-grained regolith layer with a lower

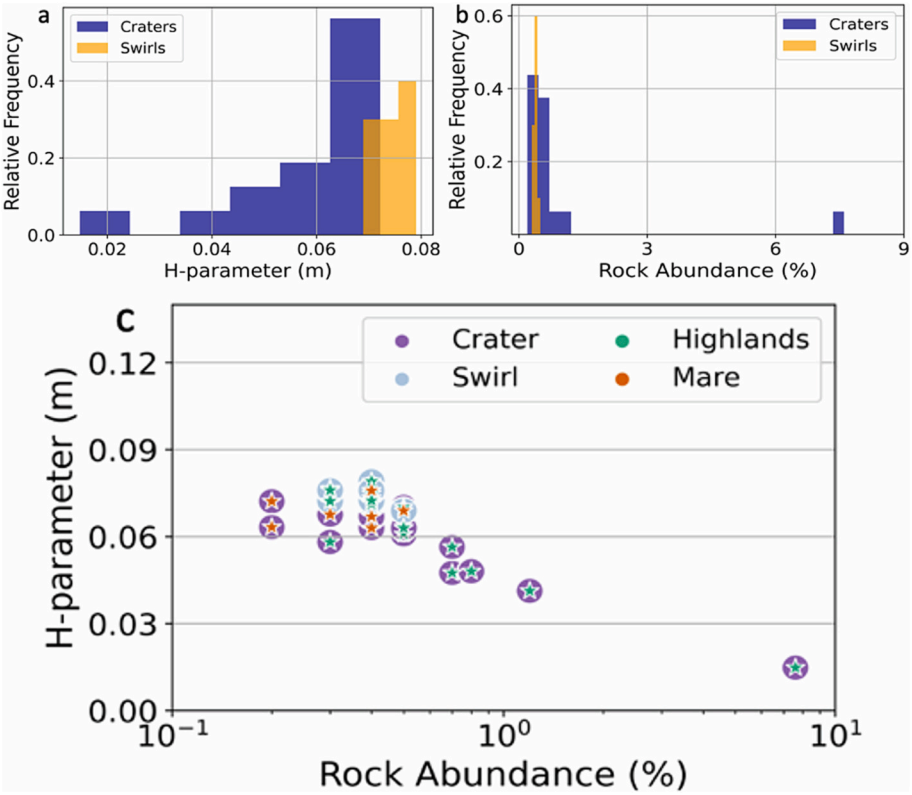

Fig. 10. a) H-parameter values observed on swirl and crater rays b)Rock abundance (%) values observed on swirl and crater rays b) H-parameter Vs RA values for crater rays and swirls.

abundance of small rocks or an increased porosity. Our observation of lower RA and higher H-parameter values on the on-swirl regions are similar to that observed by Byron et al. (2022) at irregular mare patches.

5.2. CF variation between Mare and Highlands

Fig. 11a shows that the CF variation vs albedo variation trend has a steeper slope for mare regions compared to highlands regions. Thus, for quantitatively similar variations in CF position, highland regions undergo higher albedo variation than mare (Fig. 11a). That is, if we choose a range of CF variation, the albedo variation will be higher for highlands compared to mare. Fig. 11b demonstrates that the CF variation for swirls is lower for the crater rays for similar albedo variation, i.e., if we select a range of albedo variation, the CF variation for crater rays will be higher than for swirls. Fig. 11c shows CF variation vs OMAT variation and we do not see a clear distinction between mare and highlands regions. However, the crater rays and swirls do display opposite trends of CF variation vs OMAT variation. Mare swirls display lower CF variation compared to highland swirls for similar OMAT variation. However, in the case of craters rays, highlands crater rays have higher CF variation for comparable OMAT variation to the mare crater rays.

We know from previous studies that npFe accumulates on the outer surfaces of mineral grains (e.g., Gaffey et al., 1993; Pieters and Noble, 2016) and the mare basalts display higher peak temperatures than highlands due to their low reflectivity (Williams et al., 2017). The accumulation of npFe has a minimal effect on the reflectivity of the low-albedo regolith. However, it can noticeably decrease the reflectivity of high albedo regolith. This change in albedo increases the heat conductivity of the high albedo regolith. These observations need to be investigated from two aspects: 1) particle size and 2) albedo. Smaller particle sizes result in steeper thermal gradients (Henderson and Jakosky, 1997). However, as particle size increases this thermal gradient is not as strong.

For smaller particle sizes, high albedo anorthositic materials have higher thermal gradients compared to low albedo rocks like basaltic materials (Henderson and Jakosky, 1997). This means that the highland fine-grained particles have a steeper thermal gradient than fine grained (but darker) mare particles. So, within swirls, where the particle sizes are smaller (Garrick-Bethell et al., 2011; Chrbolková et al., 2019; Hess et al., 2020) (Fig. 11), the CF shift to longer wavelengths (for space weathered regions) is lower in mare regions compared to highland regions despite comparable changes in OMAT (Fig. 11c). The darkening of highland swirls and the change in albedo requires a relatively lower accumulation of npFe compared to mare swirls where the particles are already darker. Thus, though overall it might appear that CF variation is high for mare regions (Fig. 11a), the OMAT is also high (as seen either in Fig. 11c or as large circles of data points plotted in Fig. 11a).

For crater rays, the thermal gradient is not very high due to the greater abundance of boulders and small rocks mixed in with the regolith. The CF changes more for craters for comparable changes to albedo because it is a combined effect of albedo changes due to space weathering and particle size breakdown. So, while the solid-state greenhouse effect is dominant for finer particle sizes, the lower albedos and resultant heating of the regolith is more important for larger particle sizes. If the albedo of the regolith is higher, the overall heating will be lower and thus for comparable OMAT changes, the darker mare will have larger CF shift. This also explains the opposite trend we see in the crater rays plot of OMAT vs CF changes (Fig. 11c). This effect is also observed in the laboratory studies of Shirley et al. (2023), who show that for fine grained minerals (<32 μm) there is a shallower induced thermal gradient and significantly less variation in CF position when darkening low albedo minerals (pyroxene) than when using high albedo minerals (anorthite).

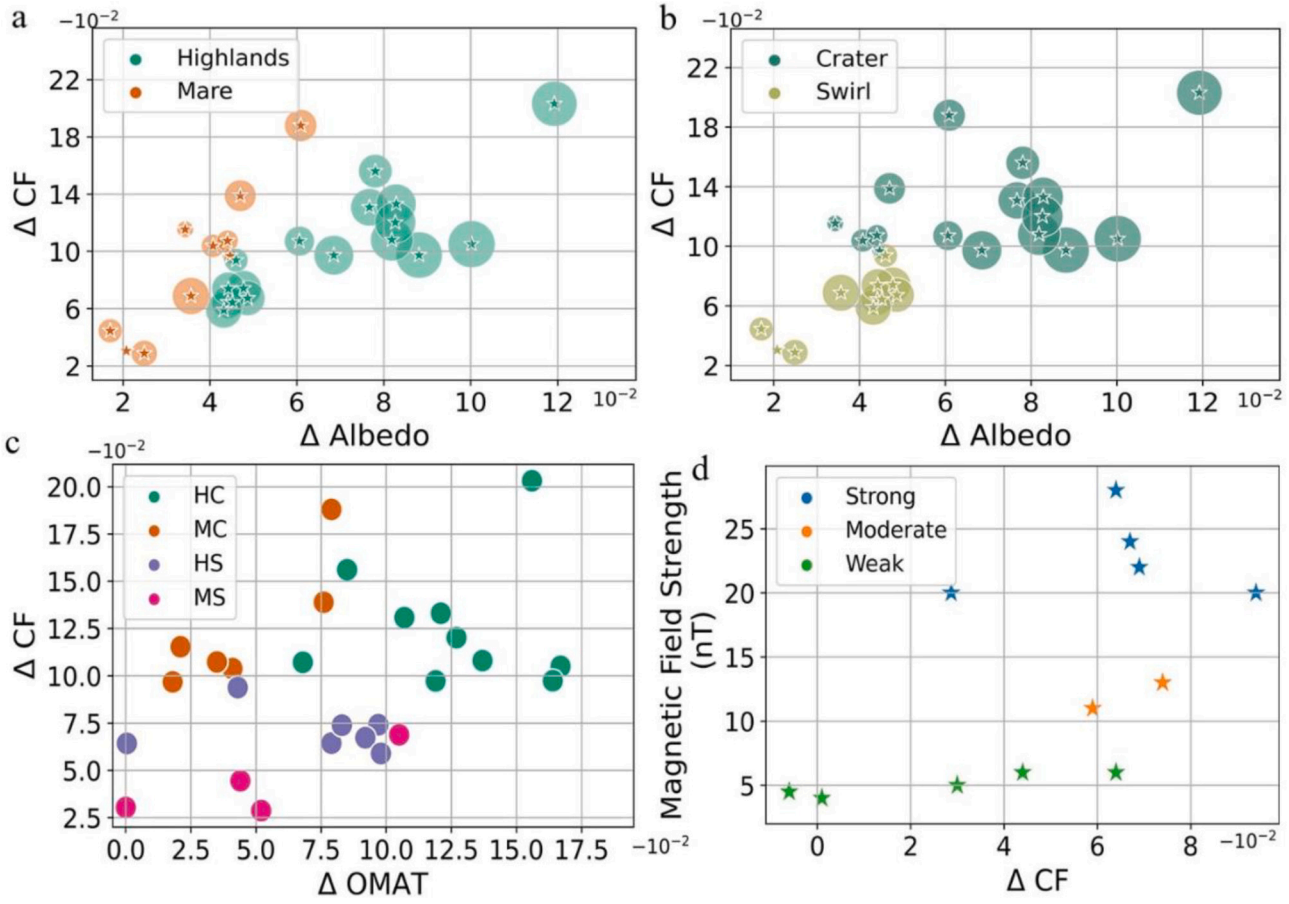

Fig. 11. a) Variation in differences of CF and albedo between ROIs at each site in the mare (orange) and highlands (green). The size of the points are representative of OMAT differences. The CF, albedo and OMAT differences have been scaled up by a factor of 10^2 and the absolute values have been taken for better visualization. b) Variation in differences of CF and albedo for swirls (light green) and craters (dark green). The size of the points are representative of OMAT differences. c) Variation in differences of CF and OMAT with respect to composition and site typed). Variation in differences of CF and magnetic field strength for lunar swirls given in Blewett et al. (2011). (For interpretation of the references to colour in this figure legend, the reader is referred to the web version of this article.)

Table 2
Magnetic field strength observed from 30 km orbit at different swirls from Blewett et al. (2011). <7 nT: Weak, 7–15 nT: Moderate, >15 nT: Strong (Blewett et al., 2011).

Name	Magnetic Field Strength(nT)	Classification
Reiner Gamma	22	Strong
Ingenii	20	Strong
Marginis	6	Weak
Firsov	11	Moderate
Descartes	24	Strong
Gerasimovich	28	Strong
Airy	13	Moderate
Marginis Highlands	6	Weak

5.3. *Effect of magnetic field strength on space weathering*

In an attempt to understand the long-term effect of magnetic shielding on the space weathering of swirls, we used the magnetic field strength (nT) values from Blewett et al. (2011) (Table 2) and compared them to the observed CF differences on the respective lunar swirls. The rms deviation of Lunar Prospector Magnetometer measurement is ~0.4nT. Fig. 11d demonstrates that stronger magnetic fields result in larger CF differences between on-swirl and off-swirl regions. We have used the highest magnetic field strength of the region for comparison, thus the outlier at 3 ΔCF, 20 nT corresponding to Mare Ingenii in the figure may not have an accurate field strength value, i.e., from the same location as the on-swirl ROI. For instance, the highest magnetic field strength in Rimae Sirsalis region is 8 nT, which is moderate, however, field strength in our ROI is only 4.5 nT, which is very weak. We haven't used the magnetic field strength of the exact ROI location because we have used the value given in Blewett et al. (2011) tables and figures. The inaccuracy in determining the exact magnetic field strength might also be responsible for the inconsistency in the values of CF for on and off-swirl regions.

6. Conclusion

In this study, we have used LRO Diviner and Kaguya MI data to determine and understand the variation in CF values with respect to space weathering and investigated the relationship between magnetic field strength and variation in space weathering.

This study demonstrates that the dark lanes in swirls are relatively immature compared to mature background regolith, indicating the magnetic field lines are not truly vertical at these locations and represent a transition zone between the high-albedo lanes of the swirls and the background regolith. By targeting high-albedo lunar swirls and rough surfaces from Copernican craters, we observe that the albedo and a combination of the abundance of small rocks, regolith porosity, or particle size distribution have a strong effect on the space weathering sequence and observed spectral properties of mature and immature surfaces. Crater rays have a higher Diviner rock abundance and lower H-parameter than similarly immature swirls, and experience a greater shift in CF. This suggests that the greater abundance of boulders/small rocks

and/or the larger average particle size distribution at crater rays causes a shift in the CF in addition to the shift caused by maturity and albedo. Though the relation between the effects of initial FeO content and particle size on space weathering trends is not yet determined, our observations indicate different behavior and phenomenon dominating the CF changes in different porosity, rock abundance and particle size ranges. This correlation with porosity, rock abundance and particle size has important implications for any proposed corrections for the effects of space weathering on CF position.

This study strongly suggests that further laboratory measurements in the simulated airless body conditions are of paramount importance for understanding the various factors affecting TIR spectra of mature and immature surfaces and for accurate interpretation of remote sensing datasets from ongoing and upcoming missions on the airless bodies. It also indicates that we may need a model that considers porosity, rock abundance and particle size distribution in addition to the initial iron content and OMAT when deriving a space weathering correction for TIR spectra of airless bodies. A machine learning model with fine and coarse particulates and space weathered spectra in its training set should be the next course of action to actively avoid correcting for each variable individually.

CRediT authorship contribution statement

Nandita Kumari: Conceptualization, Data curation, Formal analysis, Methodology, Visualization, Writing – original draft, Writing – review & editing. **Timothy D. Glotch:** Conceptualization, Funding acquisition, Investigation, Project administration, Resources, Supervision, Validation, Writing – review & editing. **Katherine A. Shirley:** Validation, Writing – review & editing. **Benjamin T. Greenhagen:** Validation, Writing – review & editing. **Benjamin D. Byron:** Writing – review & editing.

Declaration of competing interest

The authors declare no competing interests in any regard.

Data availability statement

Diviner data used in this work are available at the Planetary Data Systems Geosciences node (Paige et al., 2010). Kaguya MI data used in this work are available at JAXA website (Ohtake et al., 2008). The OMAT maps were downloaded from USGS Astrogeology page (Lemelin et al., 2015;2016). The H-parameter maps were from Hayne et al., (2017). The location is provided in table 1. Derived data products created for this work will be made available at the Mendeley Data repository at the time of publication. Currently they are temporarily available at https://data.mendeley.com/datasets/3trt7jnmwc/draft?a=e713dfad-4858-41f6-b417-433a0b2e0224 for the reviewers.

Acknowledgement

This work was supported by the Lunar Reconnaissance Orbiter Extended Science Mission under a subcontract to T.D.G. We would like to thank two anonymous reviewers for their constructive feedback which helped us improve our manuscript.

Appendix

Statistical comparison of ROIs

We binned the CF data in histograms using the Freedman-Diaconis rule (Freedman and Diaconis, 1981). This method minimizes the area between theoretical and empirical distributions, thus avoiding any binning bias in the data. The bin sizes are estimated using the following formula:

$$b = 2\,\frac{IQR(x)}{\sqrt[3]{n}} \tag{1}$$

where b is the number of bins, IQR is the interquartile range of the data, x is the pixel values in the selected ROIs and n is the number of samples (here pixels). As a result, the derived histograms do not have equal bin sizes. Equal weights have been provided to the observed pixel values to create relative frequency measurements. Bootstrapping is a standard statistical resampling method (Davison and Hinkley, 1997) that we apply to our data to understand the variations in the CF and albedo ranges. A simple difference of CF or albedo between the medians of the different regions in each site is not enough to understand the range of variations. For instance, the differences upon which we make final conclusions on should hold true for every highly statistically probable combination of the selected ROIs.

This is done in five steps:

(1) We create an array of the ROIs length (by replacement) from the ROI values of both the on and off-site individually.
(2) We calculate the median of each array for both regions of each site individually.
(3) We calculate the difference between the two medians calculated from the two ROIs of the region. The delta CF has been estimated by subtracting off-swirl/ray regions from the on-swirl/ray regions.
(4) We repeat this process for 10^5 times for each site to have a large enough statistical sample of median differences to prevent missing anything important (large variations). We have used median values because these are not affected by outliers unlike mean values.
(5) We calculate the range between the maximum and minimum median differences of CF and albedo. If this value is below 0.002 μm for CF and 0.02 for albedo, it implies the difference in median values between ROIs is statistically insignificant. If the median difference range is above that, that indicates that the variation of values in the ROI is large. That would imply that using one median value for difference estimation from each ROI is not representative of the data population.

The small ranges (on the order of 10^{-4}) for CF and albedo differences indicates that the selected median is a good representation of these surface values. Furthermore, we find that the range of median differences is below the sensitivity of each dataset and thus using one value of the difference is also statistically appropriate. The range of the median differences of CF and albedo for each site is indicated after their respective values. There is always a chance of getting different CF and albedo values arbitrarily (randomly by chance). To further test that the variation in CF at these sites is true and not arbitrary, we have carried out Kolmogorov-Smirnov (KS) tests for two samples (here the two ROIs, i.e. on and off swirl/ray) to reject the null hypothesis using KS statistics and *p*-values of the CF values from on and off swirl/crater rays. The KS test was chosen because it does not require the

data to follow any distribution.

The critical value, also known as distance statistics in the KS test can be calculated by:

$$D = c\,(\alpha)\sqrt{\frac{n_1 + n_2}{n_1 n_2}} \tag{2}$$

where D is the distance statistic,n_1 and n_2 are the sample sizes of the two samples, α is the indicator of the confidence level that the data belongs to different distribution, and c(α) corresponds to the critical value of n sample sizes at the confidence level of α. The value of α is the significance at which we want to test our data, with higher significance corresponding to lower confidence. Here we have taken α as 0.05 indicating a high confidence interval of 95% and the corresponding value of c(α) has been taken as 1.36 from statistical tables. Hence, we will have same critical value for both albedo and CF pixels of the two sites used in the testing. p-value for non-parametric two-sample tests is the probability of the data to belong to the same distribution. It is a property of the data and to reject a null hypothesis, it should always be less than the chosen value of α.

We calculated the critical value individually for each site for comparison. Our null hypothesis is that both the on-site and off-site data have the same distributions, i.e., they are not different. To investigate this, we randomly mixed the data from both the ROIs together and calculated the difference (also known as the critical value) between their cumulative distribution function. If this difference is small, that would mean that the pixel values of both the ROIs (on-swirl/ray and off-swirl/ray) are not different. However, if these values are greater than the defined distance statistics (D-statistic; calculated using the eq. (2)) then they are vastly different. We used D-statistic to reject the null hypothesis for the CF and albedo distribution observed on the on-swirl/rayed and off-swirl/rayed sites. To reject the null hypothesis, the D-statistic has to be higher than the critical value of the two samples and the p-value must be lower than the α. The p-value is rounded off to 0 if it is lower than e^{-16}. The closer the D-statistic is to 1, the higher the difference between the samples and vice-versa.

Table A1
List of the CF and albedo differences and relevant statistical values. The greater the difference between the D-statistic and the critical value, the larger is the difference between the on-site and off-site ROIs. The p-value smaller than 0.05 indicates the probability of on-site and off-site data to be from the same distribution is <5%. The starred values have not been used in the Fig. 10a and b for reasons described in Section 4.1.

Feature Name	Delta CF (μm)	Delta Albedo	Critical Value	D-Statistic (CF)	D-Statistic (Albedo)	P-value (CF)	P-value (Albedo)
Reiner Gamma	-0.07^{+}_{-} 0.0005	0.04^{+}_{-} $9.72e^{-05}$	0.0207	0.759	0.994	0.0	0.0
Mare Ingenii	-0.03^{+}_{-} 0.0006	0.03^{+}_{-} 0.0001	0.0313	0.485	0.995	$3.89e^{-10}$	0.026
Mare Marginis	-0.04^{+}_{-} 0.001	0.02^{+}_{-} $9.59e^{-05}$	0.0340	0.499	0.952	0.0	0.0
Hopmann	-0.03^{+}_{-} 0.0003	0.02^{+}_{-} 0.0001	0.0174	0.512	0.748	0.0	0.0
Moscoviense Basin*	-0.00^{+}_{-} 0.001	0.02^{+}_{-} 0.0001	0.0521	0.139	0.992	$4.73e^{-12}$	0.0
Van de Graaf	-0.07^{+}_{-} 0.0003	0.04^{+}_{-} 0.0001	0.0198	0.875	0.992	0.0	0.0
Firsov	-0.06^{+}_{-} 0.0005	0.04^{+}_{-} 0.0003	0.0437	0.931	0.989	0.0	0.0
Marginis Highlands	-0.06^{+}_{-} 0.0006	0.05^{+}_{-} 0.0003	0.0347	0.923	0.993	$7.32e^{-15}$	$7.32e^{-15}$
Ingenii Highlands	-0.09^{+}_{-} 0.0005	0.05^{+}_{-} 0.0002	0.0256	0.887	0.906	0.0	0.0
Airy	-0.07^{+}_{-} 0.0005	0.05^{+}_{-} 0.0001	0.0276	0.916	0.996	0.0	0.0
Gerasimovich	-0.06^{+}_{-} 0.0003	0.04^{+}_{-} 0.0001	0.0192	0.862	0.983	0.0	0.0
Descartes	-0.07^{+}_{-} 0.0005	0.05^{+}_{-} 0.0003	0.0237	0.909	0.933	0.0	0.0
Sirsalis*	0.01^{+}_{-} 0.0001	0.02^{+}_{-} 0.0001	0.0845	0.146	1.0	$2.53\ e^{-05}$	$2.22e^{-16}$
Kepler	-0.10^{+}_{-} 0.0002	0.04^{+}_{-} $5.15e^{-05}$	0.0119	0.938	0.999	0.0	0.0
Kepler A	-0.11^{+}_{-} 0.0002	0.04^{+}_{-} $4.79e^{-05}$	0.0123	0.979	0.999	0.0	0.0
Unnamed K	-0.14^{+}_{-} 0.001	0.05^{+}_{-} 0.0002	0.925	1.0	1.0	$2.22e^{-16}$	$2.22e^{-16}$
Unnamed E	-0.19^{+}_{-} 0.001	0.06^{+}_{-} 0.0003	0.0843	1.0	1.0	0.0	0.0
Gambart A	-0.12^{+}_{-} 0.0004	0.03^{+}_{-} $7.23e^{-05}$	0.0165	0.982	0.996	0.0	0.0
Messier	-0.04^{+}_{-} 0.0003	0.01^{+}_{-} $4.98e^{-05}$	0.0208	0.772	0.983	0.0	0.0
Dionysius	-0.10^{+}_{-} 0.0004	0.04^{+}_{-} 0.0001	0.0218	0.976	0.998	0.0	0.0
King	-0.13^{+}_{-} 0.0002	0.08^{+}_{-} 0.0001	0.0116	0.999	0.999	0.0	0.0

(continued on next page)

Table A1 (*continued*)

Feature Name	Delta CF (μm)	Delta Albedo	Critical Value	D-Statistic (CF)	D-Statistic (Albedo)	P-value (CF)	P-value (Albedo)
Necho	-0.13^{+}_{-} 0.0002	0.08^{+}_{-} $9.32e^{-05}$	0.0113	0.997	0.999	0.0	0.0
Pierazzo	-0.10^{+}_{-} 0.0003	0.09^{+}_{-} 0.0001	0.0176	0.983	1.0	0.0	0.0
Grigg E	-0.10^{+}_{-} 0.0004	0.07^{+}_{-} 0.0002	0.0232	0.957	1.0	0.0	0.0
Byrgius A	-0.11^{+}_{-} 0.0003	0.06^{+}_{-} 0.0002	0.0148	0.972	0.999	0.0	0.0
Giordano Bruno	-0.11^{+}_{-} 0.0005	0.10^{+}_{-} 0.0003	0.0250	0.955	0.999	0.0	0.0
Glushko	-0.11^{+}_{-} 0.0003	-0.11^{+}_{-} $7.86e^{-05}$	0.0136	0.997	1.0	0.0	0.0
Unnamed Crater	-0.11^{+}_{-} 0.0003	0.12^{+}_{-} 0.0004	0.038	1.0	1.0	0.0	0.0
Mandel'shtam F	-0.11^{+}_{-} 0.0003	0.08^{+}_{-} 0.0001	0.0167	0.978	0.996	0.0	0.0
Tharp	-0.12^{+}_{-} 0.0007	0.08^{+}_{-} 0.0001	0.0472	0.995	1.0	0.0	0.0

Table A2
List of the median and median difference for on - swirl/ray, off – swirl/ray OMAT, Rock Abundance and H-parameter for on-swirl/ray regions.

Feature Name	Median OMAT (On Swirl/Ray)	Median OMAT (Off Swirl/ Ray)	Delta OMAT	Median RA(%) (On Swirl/Ray)	Median H-parameter (On- swirl/ ray) (m)
Reiner Gamma	$0.27^{+}_{-}0.03$/ $0.20^{+}_{-}0.03$	$0.17^{+}_{-}0.02$	−0.11	0.004	0.075875
Mare Ingenii	$0.19^{+}_{-}0.02$	$0.14^{+}_{-}0.02$	−0.05	0.004	0.073347
Mare Marginis	$0.18^{+}_{-}0.06$	$0.14^{+}_{-}0.07$	−0.04	0.005	0.068928
Moscoviense Basin*	$0.17^{+}_{-}0.02$	$0.17^{+}_{-}0.01$	−0.002	–	–
Van de Graaf	$0.22^{+}_{-}0.02$	$0.13^{+}_{-}0.02$	−0.02	0.003	0.0759905
Firsov	$0.25^{+}_{-}0.03$/ $0.16^{+}_{-}0.02$	$0.15^{+}_{-}0.02$	−0.08	0.004	0.07903
Marginis Highlands	$0.16^{+}_{-}0.02$	$0.16^{+}_{-}0.03$	−0.1	0.004	0.072419
Ingenii Highlands	$0.21^{+}_{-}0.04$	$0.16^{+}_{-}0.03$	−0.0004	0.003	0.07658
Airy	$0.24^{+}_{-}0.02$	$0.14^{+}_{-}0.02$	−0.04	0.003	0.0722135
Gerasimovich	$0.23^{+}_{-}0.02$	$0.15^{+}_{-}0.03$	−0.09	0.004	0.074816
Descartes	$0.25^{+}_{-}0.1$	$0.16^{+}_{-}0.02$	−0.08	0.004	0.071278
Sirsalis*	$0.17^{+}_{-}0.03$	$0.15^{+}_{-}0.01$	−0.09	–	–
Kepler	$0.21^{+}_{-}0.01$	$0.17^{+}_{-}0.02$	−0.04	0.004	0.0668875
Kepler A	$0.207^{+}_{-}0.01$	$0.17^{+}_{-}0.02$	−0.03	0.003	0.067566
Unnamed K	$0.24^{+}_{-}0.02$	$0.16^{+}_{-}0.009$	−0.08	0.002	0.06324551
Unnamed E	$0.24^{+}_{-}0.01$	$0.16^{+}_{-}0.009$	−0.08	0.002	0.072155
Gambart A	$0.19^{+}_{-}0.01$	$0.17^{+}_{-}0.01$	−0.02	0.004	0.072002
Messier	$0.21^{+}_{-}0.03$	$0.15^{+}_{-}0.009$	−0.07	0.005	0.067643
Dionysius	$0.17^{+}_{-}0.01$	$0.15^{+}_{-}0.008$	−0.02	0.004	0.0629485
King	$0.28^{+}_{-}0.03$	$0.16^{+}_{-}0.02$	−0.01	0.005	0.0607725
Necho	$0.26^{+}_{-}0.02$	$0.16^{+}_{-}0.02$	−0.11	0.005	0.063226
Pierazzo	$0.33^{+}_{-}0.02$	$0.17^{+}_{-}0.01$	−0.16	0.012	0.0412435
Grigg E	$0.29^{+}_{-}0.02$	$0.17^{+}_{-}0.0$	−0.12	0.007	0.056405
Byrgius A	$0.26^{+}_{-}0.03$	$0.19^{+}_{-}0.02$	−0.07	0.005	0.06295501
Giordano Bruno	$0.36^{+}_{-}0.04$	$0.20^{+}_{-}0.02$	−0.2	0.076	0.01475
Glushko	$0.23^{+}_{-}0.02$	$0.14^{+}_{-}0.01$	−0.08	0.005	0.070151
Unnamed Crater	$0.31^{+}_{-}0.03$	$0.15^{+}_{-}0.02$	−0.15	0.008	0.0480175
Mandel'shtam F	$0.30^{+}_{-}0.05$	$0.16^{+}_{-}0.01$	−0.14	0.007	0.0474765
Tharp	$0.28^{+}_{-}0.02$	$0.15^{+}_{-}0.01$	−0.13	0.003	0.058134

References

Adams, J.B., McCord, T.B., 1971. Optical properties of mineral separates, glass, and anorthositic fragments from Apollo mare samples. In: *lunar and planetary science conference proceedings* (Vol. 2, p. 2183).

Adams, J.B., McCord, T.B., 1973. Vitrification darkening in the lunar highlands and identification of Descartes material at the Apollo 16 site. In: *lunar and planetary science conference proceedings* (Vol. 4, p. 163).

Allen, C.C., Morris, R.V., Lauer, H.V., McKay, D.S., 1993. Microscopic Iron metal on glass and minerals-a tool for studying regolith maturity. Icarus. https://doi.org/10.1006/icar.1993.1102.

Bandfield, J.L., Hamilton, V.E., Christensen, P.R., 2000. A global view of martian surface compositions from MGS-TES. Science. https://doi.org/10.1126/science.287.5458.1626.

Bandfield, J.L., Ghent, R.R., Vasavada, A.R., Paige, D.A., Lawrence, S,J., & Robinson, M. S. 2011. Lunar surface rock abundance and regolith fines temperatures derived from LRO Diviner Radiometer data. J. Geophys. Res. Planets, 116(E12).

Bart, G.D., Melosh, H.J., 2010. Distributions of boulders ejected from lunar craters. Icarus. https://doi.org/10.1016/j.icarus.2010.05.023.
Besse, S., Sunshine, J.M., Gaddis, L.R., 2014. Volcanic glass signatures in spectroscopic survey of newly proposed lunar pyroclastic deposits. J. Geophys. Res. E: Planets. https://doi.org/10.1002/2013JE004537.
Blewett, D.T., Denevi, B.W., Robinson, M.S., Ernst, C.M., Purucker, M.E., Solomon, S.C., 2010. The apparent lack of lunar-like swirls on mercury: implications for the formation of lunar swirls and for the agent of space weathering. Icarus. https://doi.org/10.1016/j.icarus.2010.03.008.
Blewett, D.T., Coman, E.I., Hawke, B.R., Gillis-Davis, J.J., Purucker, M.E., Hughes, C.G., 2011. Lunar swirls: examining crustal magnetic anomalies and space weathering trends. [dataset]. J. Geophys. Res. E: Planets. https://doi.org/10.1029/2010JE003656.
Breitenfeld, L.B., Rogers, A.D., Glotch, T.D., Hamilton, V.E., Christensen, P.R., Lauretta, D.S., Gemma, M.E., Howard, K.T., Ebel, D.S., Kim, G., Kling, A.M., 2021. Machine learning mid-infrared spectral models for predicting modal mineralogy of CI/CM chondritic asteroids and Bennu. J. Geophysi. Res. Planets 126 (12) e2021JE007035.
Bruck Syal, M., Schultz, P.H., 2015. Cometary impact effects at the moon: implications for lunar swirl formation. Icarus. https://doi.org/10.1016/j.icarus.2015.05.005.
Byron, B.D., Elder, C.M., Williams, J.P., Ghent, R.R., Gallinger, C.L., Hayne, P.O., Paige, D.A., 2022. Thermophysical properties of lunar irregular Mare patches from LRO diviner radiometer data. J. Geophys. Res.: Planets 127 (7) e2022JE007214.
Chapman, C.R., Salisbury, J.W., 1973. Comparisons of meteorite and asteroid spectral reflectivities. Icarus 19, 507–522.
Chrbolková, K., Kohout, T., Ďurech, J., 2019. Reflectance spectra of seven lunar swirls examined by statistical methods: a space weathering study. Icarus 333, 516–527.
Christensen, P.R., Bandfield, J.L., Hamilton, V.E., Howard, D.A., Lane, M.D., Piatek, J.L., Stefanov, W.L., 2000. A thermal emission spectral library of rock-forming minerals. J. Geophys. Res.: Planets 105 (E4), 9735–9739.
Collinson, D.W., 1976. Lunar science: A post-Apollo view. Phys. Earth Planet. Inter. https://doi.org/10.1016/0031-9201(76)90070-4.
Conel, J.E., 1969. Infrared Emissivities of silicates: experimental results and a cloudy atmosphere model of spectral emission from condensed particulate mediums. J. Geophys. Res. https://doi.org/10.1029/JB074i006p01614.
Cooper, B.L., Salisbury, J.W., Killen, R.M., Potter, A.E., 2002. Midinfrared spectral features of rocks and their powders. J. Geophys. Res. E: Planets. https://doi.org/10.1029/2000je001462.
Davison, A.C., Hinkley, D.V., 1997. Bootstrap Methods and their Application (Cambridge Series in Statistical and Probabilistic Mathematics, vols. No 1). Cambridge University Press.
Denevi, B.W., Robinson, M.S., Boyd, A.K., Sato, H., Hapke, B.W., Hawke, B.R., 2014. Characterization of space weathering from lunar reconnaissance orbiter camera ultraviolet observations of the moon. J. Geophys. Res. E: Planets. https://doi.org/10.1002/2013JE004527.
Denevi, B.W., Robinson, M.S., Boyd, A.K., Blewett, D.T., Klima, R.L., 2016. The distribution and extent of lunar swirls. Icarus. https://doi.org/10.1016/j.icarus.2016.01.017.
Dran, J.C., Duraud, J.P., Klossa, J., Langevin, Y., Maurette, M., 1977. Microprobe studies of space weathering effects in extraterrestrial dust grains. Philosoph Transac Royal Soc London. Series A, Math. Phys. Sci. 285 (1327), 433–439.
Ehlmann, B.L., Klima, R.L., Benett, C.L., Blaney, D., Bowles, N., Calcutt, S., Dickson, J., Donaldson Hanna, K., Edwards, C.S., Green, R., House, M.A., Klesh, A., Pieters, C., Seybold, C., Thompson, D., Williamson, W., Wood, J., 2021. Lunar Trailblazer: A pioneering smallsat for lunar water and lunar geology, 52nd LPSC, abs. #2548. https://www.hou.usra.edu/meetings/lpsc2021/pdf/1740.pdf.
Freedman, D., Diaconis, P., 1981. Z. Wahrscheinlichkeitstheorie verw Gebiete, 57, pp. 453–476.
Fuller, M., Cisowski, S.M., 1987. In: Geomagnetism, J.A., Jacobs (Eds.), Lunar paleomagnetism, vol. 2. Academic Press, Orlando, FL, pp. 307–455.
Gaffey, M.J, Bell, J.F., Brown, R.H., Burbine, T.H., Pitaek, J.L., Reed, K.L., &Chaky, D.A., 1993. Mineralogical variations within the S-type asteroid class. Icarus 106 (2), 573–602.
Garrick-Bethell, I., Head III, J.W., Pieters, C.M., 2011. Spectral properties, magnetic fields, and dust transport at lunar swirls. Icarus 2012, 480–492. https://doi.org/10.1016/j.icarus.2010.11.036.
Glotch, T.D., Bandfield, J.L., Lucey, P.G., Hayne, P.O., Greenhagen, B.T., Arnold, J.A., Ghent, R.R., Paige, D.A., 2015. Formation of lunar swirls by magnetic field standoff of the solar wind. Nat. Commun. https://doi.org/10.1038/ncomms7189.
Gold, T., 1955. The lunar surface. Mon. Not. R. Astron. Soc. 115, 585–604.
Green, R.O., Pieters, C., Mouroulis, P., Eastwood, M., Boardman, J., Glavich, T., Isaacson, P., Annadurai, M., Besse, S., Barr, D., Buratti, B., Cate, D., Chatterjee, A., Clark, R., Cheek, L., Combe, J., Dhingra, D., Essandoh, V., Geier, S., Wilson, D., 2011. The moon mineralogy mapper (M3) imaging spectrometer for lunar science: instrument description, calibration, on-orbit measurements, science data calibration and on-orbit validation. J. Geophys. Res. E: Planets. https://doi.org/10.1029/2011JE003797.
Greenhagen, B.T., Lucey, P.G., Wyatt, M.B., Glotch, T.D., Allen, C.C., Arnold, J.A., Bandfield, J.L., Bowles, N.E., Hanna, K.L.D., Hayne, P.O., Song, E., Thomas, I.R., Paige, D.A., 2010. Global silicate mineralogy of the moon from the diviner lunar radiometer. Science. https://doi.org/10.1126/science.1192196.
Greenhagen, B.T., Lucey, P.G., Bandfield, J.L., Hayne, P.O., Williams, J.P., Paige, D.A., 2011. The diviner lunar radiometer compositional data products: description and examples. In: *lunar and planetary science conference 2011* (no. 1608, p. 2679).
Grier, J.A., McEwen, A.S., Lucey, P.G., Milazzo, M., Strom, R.G., 2001. Optical maturity of ejecta from large rayed lunar craters. J. Geophys. Res. E: Planets. https://doi.org/10.1029/1999JE001160.
Hapke, B.W., 1998. The Vapor Deposition Model of Space Weathering: A Strawman Paradigm for the Moon. Integrated Remotely Sensed, Geophysical, and Sample Datasets, New Views of the Moon, p. 34.
Hayne, P.O., Bandfield, J.L., Siegler, M.A., Vasavada, A.R., Ghent, R.R., Williams, J.P., Paige, D.A., 2017. Global regolith thermophysical properties of the moon from the diviner lunar radiometer experiment. J. Geophys. Res.: Planets 122 (12), 2371–2400. https://github.com/phayne/heat1d.
Hemingway, D., Garrick-Bethell, I., 2012. Magnetic field direction and lunar swirl morphology: insights from airy and Reiner gamma. J. Geophys. Res. Oceans. https://doi.org/10.1029/2012JE004165.
Hemingway, D.J., Tikoo, S.M., 2018. Lunar swirl morphology constrains the geometry, magnetization, and origins of lunar magnetic anomalies. J. Geophys. Res.: Planets. https://doi.org/10.1029/2018JE005604.
Henderson, B.G., Jakosky, B.M., 1997. Near-surface thermal gradients and mid-IR emission spectra: a new model including scattering and application to real data. J. Geophys. Res. E: Planets. https://doi.org/10.1029/96JE03781.
Hess, M., Wöhler, C., Bhatt, M., Berezhnoy, A.A., Grumpe, A., Wohlfarth, K., Bhardwaj, A., Shevchenko, V.V., 2020. Processes governing the VIS/NIR spectral reflectance behavior of lunar swirls. Astron. Astrophys. 639, A12.
Hiesinger, H., Helbert, J., 2010. The mercury radiometer and thermal infrared spectrometer (MERTIS) for the BepiColombo mission. Planet. Space Sci. https://doi.org/10.1016/j.pss.2008.09.019.
Hood, L.L., Schubert, G., 1980. Lunar magnetic anomalies and surface optical properties. Science. https://doi.org/10.1126/science.208.4439.49.
Hood, L.L., Williams, C.R., 1989. The lunar swirls: distribution and possible origins. In: Proc. 19th lunar and planetary science conference.
Isaacson, P.J., Pieters, C.M., Besse, S., Clark, R.N., Head, J.W., Klima, R.L., Mustard, J.F., Petro, N.E., Staid, M.I., Sunshine, J.M., Taylor, L.A., Thaisen, K.G., Tompkins, S., 2011. Remote compositional analysis of lunar olivine-rich lithologies with moon mineralogy mapper (M3) spectra. J. Geophys. Res. E: Planets. https://doi.org/10.1029/2010JE003731.
Klima, R.L., Pieters, C.M., Boardman, J.W., Green, R.O., Head, J.W., Isaacson, P.J., Mustard, J.F., Nettles, J.W., Petro, N.E., Staid, M.I., Sunshine, J.M., Taylor, L.A., Tompkins, S., 2011. New insights into lunar petrology: distribution and composition of prominent low-ca pyroxene exposures as observed by the moon mineralogy mapper (M3). J. Geophys. Res. E: Planets. https://doi.org/10.1029/2010JE003719.
Lauretta, D.S., DellaGiustina, D.N., Bennett, C.A., et al., 2019. The unexpected surface of asteroid (101955) Bennu. Nature 568, 55–60. https://doi.org/10.1038/s41586-019-1033-6.
Logan, L.M., Hunt, G.R., Salisbury, J.W., Balsamo, S.R., 1973. Compositional implications of Christiansen frequency maximums for infrared remote sensing applications. J. Geophys. Res. https://doi.org/10.1029/jb078i023p04983.
Lucey, P.G., Blewett, D.T., Jolliff, B.L., 2000a. Lunar iron and titanium abundance algorithms based on final processing of Clementine ultraviolet-visible images. J. Geophys. Res. E: Planets. https://doi.org/10.1029/1999JE001117.
Lucey, P.G., Blewett, D.T., Taylor, G.J., Hawke, B.R., 2000b. Imaging of lunar surface maturity. J. Geophys. Res.: Planets 105 (E8), 20377–20386.
Lucey, P.G., Greenhagen, B., Donaldson Hanna, K., Bowles, N., Flom, A., Paige, D.A., 2021. Christiansen feature map from the lunar reconnaisance orbiter diviner lunar radiometer experiment:improved corrections and derived mineralogy. J. Geophys. Res. Planets 126 e2020JE006777.
Lucey, P.G., Greenhagen, B.T., Song, E., Arnold, J.A., Lemelin, M., Hanna, K.D., Bowles, N.E., Glotch, T.D., Paige, D.A., 2017. Space weathering effects in diviner lunar radiometer multispectral infrared measurements of the lunar Christiansen feature: characteristics and mitigation. Icarus. https://doi.org/10.1016/j.icarus.2016.05.010.
Mighani, S., Wang, H., Shuster, D.L., Borlina, C.S., Nichols, C.I.O., Weiss, B.P., 2020. The end of the lunar dynamo. Sci. Adv. https://doi.org/10.1126/sciadv.aax0883.
Namur, O., Charlier, B., 2017. Silicate mineralogy at the surface of mercury. Nat. Geosci. https://doi.org/10.1038/ngeo2860.
Neumann, G.A., et al., 2015. Copernican-Age Craters and LOLA Decameter-Scale Roughness, 46th Lunar and Planetary Science Conference, Abstract #2218.
Noble, S.K., Pieters, C.M., Keller, L.P., 2007. An experimental approach to understanding the optical effects of space weathering. Icarus. https://doi.org/10.1016/j.icarus.2007.07.021.
Ohtake, M., Haruyama, J., Matsunaga, T., Yokota, Y., Morota, T., Honda, C., the LISM team, 2008. Performance and scientific objectives of the SELENE (KAGUYA) multiband imager. Earth Planets Space 60, 257–264. https://data.darts.isas.jaxa.jp/pub/pds3/sln-l-mi-5-map-v3.0/.
Paige, D.A., Foote, M.C., Greenhagen, B.T., Schofield, J.T., Calcutt, S., Vasavada, A.R., Preston, D.J., Taylor, F.W., Allen, C.C., Snook, K.J., Jakosky, B.M., Murray, B.C., Soderblom, L.A., Jau, B., Loring, S., Bulharowski, J., Bowles, N.E., Thomas, I.R., Sullivan, M.T., McCleese, D.J., 2010. The lunar reconnaissance orbiter diviner lunar radiometer experiment. Space Sci. Rev. https://doi.org/10.1007/s11214-009-9529-2 [Dataset] https://pds-geosciences.wustl.edu/lro/lro-l-dlre-4-rdr-v1/lrodlr_1001/data/gdr_l3/.
Pieters, Carle M., Noble, S.K., 2016. Space weathering on airless bodies. J. Geophys. Res.: Planets. https://doi.org/10.1002/2016JE005128.
Pieters, C.M., Taylor, L.A., Noble, S.K., Keller, L.P., Hapke, B., Morris, R.V., Wentworth, S., 2000. Space weathering on airless bodies: resolving a mystery with lunar samples. Meteorit. Planet. Sci. 35 (5), 1101–1107.
Pieters, C.M., Boardman, J.W., Burratti, B., Clark, R.N., Combe, J.P., Green, R.O., Head, J.W., Hicks, M., Isaacson, P., Klima, R.L., Kramer, G.Y., Lundeen, S.,

Malaret, E., McCord, T.B., Mustard, J.F., Nettles, J.W., Petro, N.E., Runyon, C.J., Staid, M., Varanasi, P., 2009. New mg-Spinel Rock-Type on the Lunar Farside and Implications for Lunar Crustal Evolution (AGU Fall Meeting).

Pieters, C.M., Garrick-Bethell, I., Hemingway, D., 2014. Magnetic Sorting of the Regolith on the Moon: Lunar Swirls. AGU Fall Meeting, Abs, pp. P11D–10.

Poppe, A.R., Farrell, W.M., Halekas, J.S., 2018. Formation timescales of amorphous rims on lunar grains derived from ARTEMIS observations. J. Geophys. Res.: Planets. https://doi.org/10.1002/2017JE005426.

Prem, Parvathy, et al., 2022. Modeling thermal emission under lunar surface environmental conditions. Planet. Sci. J. 3 (7), 180.

Prinz, M., Dowty, E., Keil, K., Bunch, T.E., 1973. Spinel troctolite and anorthosite in Apollo 16 samples. Science 179 (4068), 74–76.

Robinson, M.S., Brylow, S.M., Tschimmel, M., Humm, D., Lawrence, S.J., Thomas, P.C., Denevi, B.W., Bowman-Cisneros, E., Zerr, J., Ravine, M.A., Caplinger, M.A., Ghaemi, F.T., Schaffner, J.A., Malin, M.C., Mahanti, P., Bartels, A., Anderson, J., Tran, T.N., Eliason, E.M., Hiesinger, H., 2010. Lunar reconnaissance orbiter camera (LROC) instrument overview. Space Sci. Rev. https://doi.org/10.1007/s11214-010-9634-2.

Salisbury, J.W., D'Aria, D.M., Jarosewich, E., 1991. Midinfrared (2.5-13.5μm) reflectance spectra of powdered meteorites. Icarus 92 (2), 280–297.

Schultz, P.H., Srnka, L.J., 1980. Cometary collisions on the moon and mercury. Nature. https://doi.org/10.1038/284022a0.

Shirley, K.A., 2018. The Effects of Particle Size and Albedo on Mid-Infrared Spectroscopy for the Moon (Doctoral dissertation,. State University of New York at Stony Brook. https://ui.adsabs.harvard.edu/abs/2018PhDT.....102S/abstract.

Shirley, K.A., Glotch, T.D., 2019. Particle size effects on mid-infrared spectra of lunar analog minerals in a simulated lunar environment. J. Geophys. Res.: Planets. https://doi.org/10.1029/2018JE005533.

Shirley, K.A., Glotch, T.D., Donaldson, O., Trelewicz, J., Yang, Y., Zhang, H., 2023. Effects of albedo on the MIR emissivity of silicates for lunar Comarison. J. Geophys. Res.: Planets. https://doi.org/10.1029/2022JE007629.

Shoemaker, E.M., Hackman, R.J., 1962. Stratigraphic basis for a lunar time scale. Symp. - Int. Astron. Union. https://doi.org/10.1017/s007418090017826x.

Smith, J.V., Anderson, A.T., Newton, R.C., Olsen, E.J., Wyllie, P.J., 1970. A petrologic model for the moon based on Petrogenesis, experimental petrology, and physical properties. J. Geol. https://doi.org/10.1086/627537.

Spudis, P.D., Hawke, B.R., Lucey, P., 1984. Composition of Orientale basin deposits and implications for the lunar basin-forming process. J. Geophys. Res. https://doi.org/10.1029/jb089is01p0c197.

Staid, M.I., Pieters, C.M., Besse, S., Boardman, J., Dhingra, D., Green, R., Head, J.W., Isaacson, P., Klima, R., Kramer, G., Mustard, J.M., Runyon, C., Sunshine, J., Taylor, L.A., 2011. The mineralogy of late stage lunar volcanism as observed by the moon mineralogy mapper on Chandrayaan-1. J. Geophys. Res. E: Planets. https://doi.org/10.1029/2010JE003735.

Starukhina, L.V., Shkuratov, Y.G., 2004. Swirls on the moon and mercury: meteoroid swarm encounters as a formation mechanism. Icarus. https://doi.org/10.1016/j.icarus.2003.08.022.

Taylor, S.R., Siscoe, G.L., 1976. Lunar science: a post-Apollo view. Phys. Today. https://doi.org/10.1063/1.3023321.

Tikoo, S.M., Weiss, B.P., Shuster, D.L., Suavet, C., Wang, H., Grove, T.L., 2017. A two-billion-year history for the lunar dynamo. Sci. Adv. https://doi.org/10.1126/sciadv.1700207.

Trang, D., Lucey, P.G., 2019. Improved space weathering maps of the lunar surface through radiative transfer modeling of Kaguya multiband imager data. Icarus 321, 307–323.

Trang, D., Lucey, P.G., Izenberg, N.R., 2017. Radiative transfer modeling of MESSENGER VIRS spectra: detection and mapping of submicroscopic iron and carbon. Icarus 293, 206–217.

Weiss, B.P., Tikoo, S.M., 2014. The lunar dynamo. Science. https://doi.org/10.1126/science.1246753.

Wentworth, S.J., Keller, L.P., McKay, D.S., Morris, R.V., 1999. Space weathering on the moon: Patina on Apollo 17 samples 75075 and 76015. Meteorit. Planet. Sci. 34 (4), 593–603.

Werner, S.C., Medvedev, S., 2010. The lunar rayed-crater population—characteristics of the spatial distribution and ray retention. Earth Planet. Sci. Lett. 295 (1–2), 147–158.

Williams, J-P, Paige, D.A., Greenhagen, B.T., Sefton-Nash, E., 2017. The global surface temperatures of the moon as measured by the diviner lunar radioemeter experiment. Icarus 283, 300–325.

Wilshire, H.G., Jackson, E.D., 1972. Lunar "dunite","pyroxenite" and "anorthosite". Earth Planet. Sci. Lett. 16 (3), 396–400.

Wood, J.A., Dickey Jr., J.S., Marvin, U.B., Powell, B.N., 1970. Lunar anorthosites and a geophysical model of the moon. Geochim. Cosmochim. Acta 1, 965.

Zeller, E.J., Ronca, L.B., 1967. Space weathering of lunar and asteroidal surfaces. Icarus 7 (1–3), 372–379.